JACS
JOURNAL OF THE AMERICAN CHEMICAL SOCIETY

Article

pubs.acs.org/JACS

# Successive Stages of Amyloid-$\beta$ Self-Assembly Characterized by Solid-State Nuclear Magnetic Resonance with Dynamic Nuclear Polarization

Alexey Potapov,[†] Wai-Ming Yau,[†] Rodolfo Ghirlando,[‡] Kent R. Thurber,[†] and Robert Tycko*[,†]

[†]Laboratory of Chemical Physics and [‡]Laboratory of Molecular Biology, National Institute of Diabetes and Digestive and Kidney Diseases, National Institutes of Health, Bethesda, Maryland 20892-0520, United States

Supporting Information

**ABSTRACT:** Self-assembly of amyloid-$\beta$ (A$\beta$) peptides in human brain tissue leads to neurodegeneration in Alzheimer's disease (AD). Amyloid fibrils, whose structures have been extensively characterized by solid state nuclear magnetic resonance (ssNMR) and other methods, are the thermodynamic end point of A$\beta$ self-assembly. Oligomeric and protofibrillar assemblies, whose structures are less well-understood, are also observed as intermediates in the assembly process in vitro and have been implicated as important neurotoxic species in AD. We report experiments in which the structural evolution of 40-residue A$\beta$ (A$\beta$40) is monitored by ssNMR measurements on frozen solutions prepared at four successive stages of the self-assembly process. Measurements on transient intermediates are enabled by ssNMR signal enhancements from dynamic nuclear polarization (DNP) at temperatures below 30 K. DNP-enhanced ssNMR data reveal a monotonic increase in conformational order from an initial state comprised primarily of monomers and small oligomers in solution at high pH, to larger oligomers near neutral pH, to metastable protofibrils, and finally to fibrils. Surprisingly, the predominant molecular conformation, indicated by $^{13}$C NMR chemical shifts and by side chain contacts between F19 and L34 residues, is qualitatively similar at all stages. However, the in-register parallel $\beta$-sheet supramolecular structure, indicated by intermolecular $^{13}$C spin polarization transfers, does not develop before the fibril stage. This work represents the first application of DNP-enhanced ssNMR to the characterization of peptide or protein self-assembly intermediates.

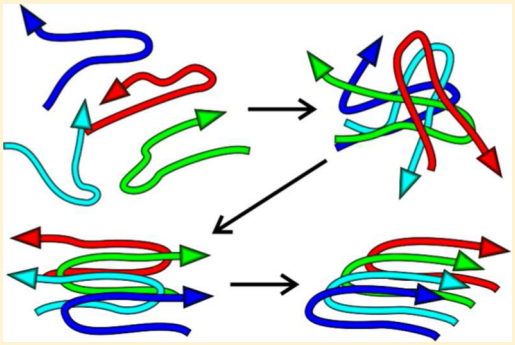

## INTRODUCTION

The detailed molecular basis for Alzheimer's disease (AD) is still largely unknown. The amyloid cascade hypothesis relates disease onset and progression to a dysregulation of amyloid-$\beta$ (A$\beta$) peptide production and clearance that leads to A$\beta$ self-assembly in brain tissue.[1] Amyloid fibrils, consisting primarily of 40- and 42-residue A$\beta$ peptides (A$\beta$40 and A$\beta$42), are the thermodynamic end point of the A$\beta$ self-assembly process and comprise the major component of self-assembled A$\beta$ in the brain tissue of AD patients. However, the total quantity of fibrillar A$\beta$ in brain tissue does not correlate strongly with the progression of neurodegeneration, as indicated by studies of human brain extracts[2] and transgenic mice.[3] Polymorphism of A$\beta$ fibrils[4] may be one factor that weakens this correlation because several types of experiments indicate that different polymorphs can have different neurodegenerative effects.[5] Alternatively, nonfibrillar A$\beta$ assemblies may be important neurotoxic species, as suggested by a variety of observations in humans and mouse models.[2,6] Nonfibrillar assemblies include oligomers of various sizes and shapes[7] as well as "protofibrils", which are metastable, fibril-like assemblies with greater curvature and shorter typical lengths.[8] Oligomers produced by aggregation of synthetic A$\beta$ peptides in vitro show higher toxicity in cell cultures than an equivalent mass of fibrils.[7d,9] Given the diversity of neurotoxicity mechanisms proposed for A$\beta$ assemblies in AD, including membrane disruption,[10] interactions with specific cell-surface receptors,[11] oxidative damage associated with binding of metal ions,[12] stimulation of destructive inflammation,[13] and disruption of vasculature,[14] it is conceivable that both fibrillar and nonfibrillar species contribute significantly to neurodegeneration, possibly through different mechanisms. Thus, characterization of A$\beta$ structures at all stages of self-assembly is an important goal.

Detailed structural models for A$\beta$ fibrils have been developed from a variety of experimental measurements, especially solid state nuclear magnetic resonance (ssNMR).[5a,15] In these models, molecules with approximately U-shaped conformations stack in an in-register parallel manner, forming parallel cross-$\beta$ structures.[4,16] Structurally distinct, self-propagating fibril polymorphs[5b] differ in the detailed conformations at certain sites, the number of cross-$\beta$ units within the minimal fibril structure, the contacts between cross-$\beta$ units, and other features. For example, salt-bridge interactions between oppositely charged D23 and K28 side chains have been

**Received:** May 9, 2015
**Published:** June 12, 2015





DOI: 10.1021/jacs.5b04843
J. Am. Chem. Soc. 2015, 137, 8294−8307

observed by ssNMR in some Aβ40 fibril polymorphs,[5a,15a] but not in other polymorphs.[15b]

A detailed molecular structural model for protofibrils formed by the Asp23-to-Asn "Iowa mutant" (D23N-Aβ40) has been developed from ssNMR data,[17] showing that U-shaped D23N-Aβ40 molecules stack in an antiparallel manner to form a double-layered, antiparallel cross-β structure in the protofibrils. In contrast, D23N-Aβ40 fibrils contain double-layered, parallel cross-β structural motifs.[15f]

Various other oligomeric and protofibril Aβ assemblies, prepared under a variety of conditions, have been partially characterized by ssNMR. These include approximately spherical Aβ40 and Aβ42 assemblies that form in aqueous buffers,[7c,d,18] Aβ42 oligomers prepared by dialysis of a detergent solution,[7b] Aβ40 protofibrils stabilized by interaction with the B10AP antibody,[19] small disc-like Aβ42 oligomers,[20] and Aβ40 oligomers formed in the presence of epigallocatechin-3-gallate (EGCG).[21] In addition, oligomers formed by a GroES-ubiquitin-Aβ42 fusion protein have been studied by electron paramagnetic resonance with spin-labeling.[22] A structural model for protofibrils formed by an internally cross-linked, double cysteine mutant of Aβ42 has also been developed from ssNMR data.[23] The consensus of these studies is that Aβ conformations in oligomers and protofibrils are similar to Aβ conformations in fibrils although the supramolecular organization may be rather different.

To date, most ssNMR studies of Aβ self-assembly intermediates have been performed on samples that were concentrated by lyophilization after oligomer formation.[7b−d,17c,18a,19,20,23] Lyophilization has been required because Aβ concentrations in oligomer preparations in vitro are typically on the order of 1 mM or less. With typical ssNMR sample volumes in the 10−100 μL range, the quantity of Aβ in the oligomer solution is then on the order of 100 nmol or less. Although ssNMR measurements can be performed successfully on frozen solutions of peptides and proteins,[24] higher concentrations and/or larger sample volumes are needed for adequate signal-to-noise, even with measurement times of several days or more. Lyophilization allows greater quantities of Aβ assemblies to be packed into smaller volumes, greatly accelerating data acquisition.

It is well-established that lyophilization does not perturb the molecular structures of amyloid fibrils significantly because NMR chemical shifts of lyophilized and lyophilized/rehydrated fibril samples are the same as those of nonlyophilized, as-grown samples.[25] For certain Aβ oligomers and protofibrils, evidence has been presented that lyophilization also does not perturb molecular structures significantly.[7c,d,17c,18a] However, in the case of smaller Aβ assemblies and assemblies that are not metastable, lyophilization may produce significant changes in molecular conformations, intermolecular interactions, and assembly sizes.

In the experiments described below, we use dynamic nuclear polarization (DNP) to enhance the sensitivity of ssNMR measurements on frozen solutions of Aβ assemblies, thereby avoiding the need for lyophilization and permitting measurements on transient species. DNP is an effect in which microwave irradiation of electron spin transitions leads to large enhancements of spin polarizations of nuclei, and hence large enhancements of ssNMR signals.[26] In recent ssNMR studies, DNP has been applied to membrane proteins,[27] amyloid fibrils,[28] and viral DNA.[29] To our knowledge, the experiments described below represent the first application of DNP in ssNMR studies of transient or metastable species with biological or biophysical relevance.

We describe experiments on four successive stages of Aβ40 self-assembly: (1) Freshly prepared Aβ40 solution at pH 12, where the peptide is primarily monomeric. (2) The same solution shortly after adjustment to pH 7.5, where the peptide exists as a mixture of monomers and oligomers of various sizes and morphologies. (3) The same solution after incubation at pH 7.5 for at least 4 h, at which time metastable Aβ40 protofibrils are the predominant species. (4) Aβ40 fibrils that develop from protofibrils during repetitive sonication/incubation cycles. Our ssNMR data indicate a progressive reduction in conformational disorder as self-assembly proceeds through these four stages. The predominant molecular conformation, indicated by $^{13}C$ chemical shifts, is qualitatively similar at all stages. Long-range tertiary contacts between side chains of F19 and L34, which are known to be a characteristic feature of many Aβ40[5a,15a,b] and Aβ42[20] fibril polymorphs, are also detectable at all stages. Surprisingly, these contacts are most pronounced at the protofibril stage. We find that parallel intermolecular alignment in Aβ40 assemblies does not develop until the fibril stage.

## METHODS

**Peptide Synthesis.** Aβ40 was synthesized on a 0.15 mmol scale by fluorenylmethoxycarbonyl (FMOC) chemistry on a Tribute TPS-110 automated peptide synthesizer (Protein Technologies), with activation by O-(6-chlorobenzotriazol-1-yl)-N,N,N′,N′-tetramethyluronium hexafluorophosphate (HCTU) and N,N-diisopropylethylamine (DIPEA) and FMOC-Wang resins (0.27 mEq/g substitution). Isotopic-labeling patterns of Aβ40 samples for ssNMR measurements are summarized in Table 1. Valine residues were deuterated to reduce the intrinsic $^{1}H$ spin−lattice relaxation rates within Aβ40 assemblies and thereby increase DNP signal enhancements. To improve yields, pseudoproline dipeptides were used at D7−S8 and G25−S26. Isotopically labeled residues were double-coupled (2 h of coupling with labeled amino acid in 4-fold excess, followed by 1 h of coupling with unlabeled amino acid in 10-fold excess). The crude product was purified by reverse-phase high-performance liquid chromatography, using a water/acetonitrile gradient with 1% acetic acid and a C3 preparative column at room temperature. Purity is estimated to be greater than 95% by mass spectrometry. For samples II−IV, the synthesis was performed up to the $^{13}C$-labeled residue (i.e., A21, A30, or G33), and then half of the resin was removed from the reaction vessel, the carbonyl-labeled amino acid coupled in the reaction vessel for 2 h, the uncoupled resin returned to the reaction vessel, the aliphatic-labeled amino acid coupled for 2 h, and unlabeled amino acid coupled for 1 h. The ratio of carbonyl-labeled to aliphatic-labeled peptides in the final product was determined from 1D NMR spectra in dimethyl sulfoxide (DMSO) solution.

**Table 1. Isotopic Labeling Patterns of Peptide Samples for ssNMR Measurements[a]**

| peptide sample | labeling of component A | labeling of component B | A:B ratio |
|---|---|---|---|
| Aβ40 I | U−$^{15}N$,$^{13}C$ at F19, L34, G38; $^{13}CO$ at A30 | U−$^{15}N$,$^{13}C$ at F19, L34, G38; $^{13}C_{\beta}$ at A30 | 50:50 |
| Aβ40 II | $^{13}CO$ at A21 | $^{13}C_{\beta}$ at A21 | 28:72 |
| Aβ40 III | $^{13}CO$ at A30 | $^{13}C_{\beta}$ at A30 | 56:44 |
| Aβ40 IV | $^{13}CO$ at G33 | $^{13}C_{\alpha}$ at G33 | 40:60 |
| $A\beta_{11-25}$ | $^{13}CO$ at F20; $^{13}C_{\beta}$ at A21; $^{15}N$ at L17 | | |

[a]All Aβ40 samples were also perdeuterated at V12, V18, V24, V36, and V39.



DOI: 10.1021/jacs.5b04843
J. Am. Chem. Soc. 2015, 137, 8294−8307

**Aβ40 Self-Assembly Protocols.** To produce the four types of Aβ40 assemblies examined in this work, purified, lyophilized peptide was first disaggregated by dissolution in hexafluoroisopropanol (HFIP) to a concentration of 2 mg/mL, incubation at room temperature for 0.5−1.0 h, and lyophilization again. HFIP-treated peptide was then dissolved at 2.5 mM concentration in 20 mM NaOH, pH ∼12. Negatively stained transmission electron microscope (TEM) images of this high-pH sample, on grids that were prepared within 2 min of peptide dissolution, showed a nearly clear TEM grid surface, with a low coverage of amorphous aggregates that may develop during drying of the grid (Figure 1A). The pH was then lowered by addition of 250 mM phosphate (pH 7.4) in a 1:4 ratio, bringing the final buffer concentration to 50 mM. A small quantity of concentrated HCl was added to adjust the final pH to 7.5. TEM images of this neutral-pH sample, on grids that were prepared within 2 min of pH adjustment, showed a high density of irregularly shaped assemblies (Figure 1B). After quiescent incubation at 24 °C for 4−5 h, a high density of relatively short and curved protofibrils was observed by TEM (Figure 1C). These structures were stable for at least several weeks in quiescent solutions at pH 7.5. After sonication of the protofibril solution (Branson S-250A sonifier, 10% duty cycle, lowest power setting, 50 pulses) and incubation at 24 °C for 12 h, TEM images showed a mixture of protofibrils and thicker, longer, and less curved fibrils. After 3−4 repetitions of the sonication/incubation procedure, conversion to mature fibrils was complete (Figure 1D).

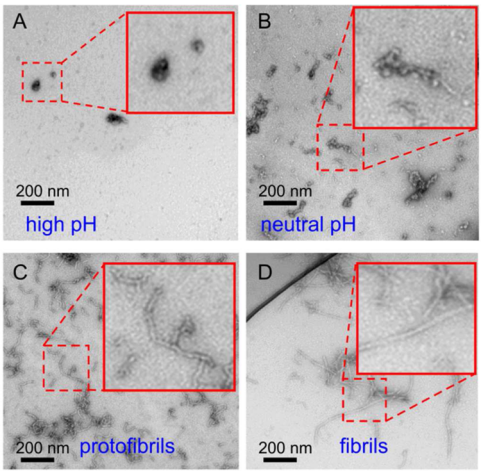


**Figure 1.** Negatively stained TEM images of Aβ40 at four stages of self-assembly. (A) High-pH sample, after initial preparation of an Aβ40 solution at pH 12. (B) Neutral pH sample, shortly after adjustment to pH 7.5. (C) Protofibril sample, after 4 h of incubation at pH 7.5. (D) Fibril sample, after four rounds of sonication and incubation. Insets are expanded views of the indicated regions.

Thioflavin T (ThT) fluorescence measurements of Aβ40 solutions (Figure S1) showed a lag period of 1.0 h after adjustment to pH 7.5, followed by an increase in fluorescence that corresponds to the development of the protofibrillar assemblies seen by TEM. The fluorescence level reached a plateau after approximately 10 h, at which time the fluorescence level was about 40% of the level observed after conversion of protofibrils to mature fibrils by sonication/incubation. Thus, it appears that nonfibrillar Aβ40 assemblies in our experiments are not ThT-active, whereas protofibrils exhibit ThT fluorescence lower than that of fibrils.

In addition, Aβ40 fibrils were prepared by seeded growth from preformed fibrils with the threefold-symmetric structure reported by Paravastu et al.[15b] Seeds were prepared by sonication of a solution of preformed fibrils. A 6 mM solution of Aβ40 in DMSO was diluted into 10 mM sodium phosphate buffer, pH 7.4, to create a 100 μM Aβ40 solution. Seeds were added in a 1:19 molar ratio (by Aβ40 monomers), and the mixture was gently vortexed. After 1 h of incubation, a 10% aliquot of the mixture was withdrawn, sonicated, and returned to the mixture. After overnight incubation, abundant fibrils were visible by TEM.

**Biophysical Characterization of Aβ40 Assemblies.** TEM images were obtained with an FEI Morgagni microscope, operating at 80 kV. Grids were glow-discharged carbon films, supported by lacey carbon on 300 mesh copper. Samples were diluted 10-fold in their own solvents (20 mM NaOH or 10 mM phosphate) before application of a 5 μL drop to the grid surface. After 1 min of adsorption, grids were blotted with filter paper, rinsed twice with water, stained for 30 s with 5 μL of 3% uranyl acetate, blotted, and dried in air.

Experiments with the photoinduced cross-linking of unmodified proteins (PICUP) technique[30] were performed by adding 10 μL of 1 mM tris(2,2′-bipyridyl)dichlororuthenium (Ru(II)) and 10 μL of 20 mM ammonium persulfate (APS) to 2.0 μL samples of Aβ40 assemblies. A 2.0 mM solution of the 35-residue villin headpiece subdomain protein (HP35) in 50 mM phosphate buffer, pH 7.4, was used as a nonaggregating control.[31] The mixtures were then irradiated at 24 °C for periods ranging from 0.5 s to 5 min, using the output of a 150 W incandescent fiber optic lamp (Dolan-Jenner model 180) and an electronically timed shutter (Melles-Griot model IES 3). Cross-linking reactions were then quenched immediately by adding 10 μL of 1 M dithiothreitol. Cross-linked products were analyzed by sodium dodecyl sulfate−polyacrylamide gel electrophoresis (SDS-PAGE). For SDS-PAGE, 4 μL of 20 μM cross-linked Aβ40 or HP35 was dissolved in NuPAGE LDS buffer (Life Technologies) and loaded onto a 10% NuPAGE Bis-Tris gel (Life Technologies). Gels were run in MES buffer for 40−45 min with a 80−100 mA current. Silver staining was performed with a SilverXpress kit (Life Technologies). Gel images were analyzed with ImageJ software.[32]

Dynamic light scattering (DLS) measurements at 658 nm wavelength were carried out with a DynaPro NanoStar (Wyatt Technology) instrument on undiluted samples (50 μL in Eppendorf UVettes) equilibrated at 25 °C. Light scattering autocorrelation functions were recorded for 60 s and averaged over 10 repetitions.

Sedimentation velocity experiments were conducted at 20.0 °C on a Beckman Coulter ProteomeLab XL-I analytical ultracentrifuge. High-pH samples were studied at rotor speeds of 50 000 and 60 000 rpm. Neutral-pH and protofibril samples were studied at 20 000, 40 000, 45 000, and 50 000 rpm. Samples were loaded into two-channel centerpiece cells, allowed to equilibrate at 20.0 °C for 2 h, and then analyzed at the indicated speeds. Concentrated samples of Aβ40 were loaded into 3 mm path length cells (100 μL), whereas diluted samples were loaded into 12 mm path length cells (400 μL). Data were collected using both absorbance (280 nm) and Rayleigh interference optical detection systems and analyzed in SEDFIT 14.4f[33] in terms of a continuous $c(s)$ distribution of Lamm equation solutions with a resolution of 0.05−0.10 S, depending on the extent of aggregation. Regularization was carried out using the method of maximum entropy with a confidence level of 0.68. The partial specific volume of Aβ40 was calculated in SEDNTERP (http://sednterp.unh.edu/) on the basis of the amino acid composition. The buffer density and viscosity were also calculated on the basis of their composition and sedimentation coefficients were corrected to standard conditions of 20 °C in water ($S_{20,w}$).

Thioflavin T (ThT) fluorescence measurements were performed at room temperature with a StellarNet BLACK-Comet-TEC fiber optic spectrofluorometer. For each time point, an aliquot of the Aβ40 sample was diluted by a factor of 100 with 10 mM sodium phosphate buffer (pH 7.4) containing 100 μM ThT. Fluorescence intensity at 490 nm was measured immediately after dilution, with excitation at 423 nm.

Circular dichroism (CD) spectra were recorded with a JASCO J-715 spectropolarimeter, using 0.01 mm path length quartz cuvettes. Acquisition of CD spectra began immediately after sample preparation. Three spectra of each sample were recorded in succession, with approximately 11 min acquisition time per spectrum, to confirm that the spectra did not change on the time scale of the CD measurements.

Size-exclusion chromatography (SEC) experiments were performed with a BioRAD NGC chromatography system. Aβ40 samples (50 μL injected volume) were separated at 0.5 mL/min on a Superose 6 10/


DOI: 10.1021/jacs.5b04843
J. Am. Chem. Soc. 2015, 137, 8294−8307

300 GL column (GE Healthcare), with a total column volume of $V_c$ = 24 mL. Prior to separation, the column was equilibrated with either 10 mM sodium phosphate buffer (pH 7.4) or 20 mM NaOH (with or without 150 mM NaCl). To check reproducibility, several runs were carried out for each condition, each followed by flushing with 3−4 $V_c$ to remove any residual A$\beta$40 from the column. Molecular weight calibration runs were performed with a HMW Calibration Kit (GE Healthcare).

**DNP and ssNMR Measurements.** DNP-enhanced ssNMR experiments were carried out at 9.4 T (400.9 MHz $^1$H NMR frequency, 264.0 GHz microwave frequency) using the low-temperature ssNMR and DNP instrumentation described previously.[26d,34] In brief, the home-built magic-angle-spinning (MAS) ssNMR probe used elongated MAS rotors with 4 mm outer diameter and 80 $\mu$L sample volume. Nitrogen gas was used for MAS drive and bearings, whereas the sample volume near the center of the rotor was cooled with helium from a liquid helium transfer line connected to the MAS module of the ssNMR probe. Experiments were performed at sample temperatures of 25 ± 2 K and at 6.7 kHz MAS frequency. Sample temperatures were determined from $^{79}$Br spin−lattice relaxation rates of KBr powder, contained in capillary tubes within the MAS rotors.[35] $^1$H radio frequency (rf) fields for decoupling were 80−85 kHz. $^1$H−$^{13}$C cross-polarization used $^1$H rf fields of 54 kHz and $^{13}$C rf fields of 47 kHz. $^1$H−$^{15}$N cross-polarization used $^1$H rf fields of 50 kHz and $^{15}$N rf fields of 43 kHz. $^{15}$N−$^{13}$C cross-polarization used $^{15}$N rf fields of 24 kHz and $^{13}$C rf fields of 31 kHz. An extended interaction oscillator (Communications and Power Industries) was used as the microwave source, with continuous-wave output power of approximately 1.4 W. Microwaves were circularly polarized with a quasi-optical interferometer (Thomas Keating, Ltd.) and transmitted to the sample through a corrugated waveguide within the ssNMR probe.

NMR data were collected with a Bruker Avance III spectrometer console and processed with nmrPipe,[36] Bruker Topspin, and Sparky (https://www.cgl.ucsf.edu/home/sparky) software. 2D $^{13}$C−$^{13}$C ssNMR spectra were acquired with either $^{13}$C−$^{13}$C spin diffusion or rf-assisted diffusion/dipolar-assisted rotational resonance[37] (RAD/DARR) during the mixing period between $t_1$ and $t_2$ periods. 2D $^{15}$N−$^{13}$C ssNMR spectra were acquired with 5 ms $^{15}$N−$^{13}$C band-selective cross-polarization periods and (for protofibril and fibril samples) 23.8 ms $^{13}$C−$^{13}$C spin diffusion periods between $t_1$ and $t_2$. Recycle delays were approximately 5 s for high-pH and neutral-pH samples and 10 s for protofibril and fibril samples, corresponding to approximately 1.3 times the characteristic build-up times for $^1$H spin polarizations under DNP. Total measurement times were 1.5−5 h for 2D $^{13}$C−$^{13}$C spectra and 4.5−10 h for 2D $^{15}$N−$^{13}$C spectra. In 2D measurements on high-pH and neutral-pH samples, the number of scans per $t_1$ point decreased with increasing $t_1$.[38] Measurements of intermolecular $^{13}$C polarization transfers were performed as described below, with total measurement times of 2−4 h for each sample.

For DNP-enhanced ssNMR measurements, A$\beta$40 samples in the four stages of self-assembly described above were prepared in 80% $D_2O$/20% $H_2O$ solutions because solvent deuteration is known to increase DNP signal enhancements and reduce DNP build-up times.[39] For high-pH and neutral-pH samples, $^{13}$C-depleted, perdeuterated glycerol was then added to achieve 60% (by mass) glycerol concentration, along with an aliquot of the triradical dopant DOTOPA-3OH-Methoxy[34] in perdeuterated DMSO to achieve a 6.6 mM dopant concentration. Immediately after mixing, samples were loaded into MAS rotors and frozen by immersion in liquid nitrogen. Protofibril and fibril samples were pelleted by centrifugation at 430 000 g for 2.0 h (Beckman TLA 100.2 rotor). Supernatants were removed, and glycerol and triradical dopant were added. After a second centrifugation for 2 h, pellets were loaded into MAS rotors and frozen. Final dopant concentrations in protofibril and fibril samples were approximately 1 mM. Final high-pH and neutral-pH samples for ssNMR contained 0.3 mg of A$\beta$40. Final protofibril and fibril samples contained roughly 5 mg of A$\beta$40.

## RESULTS

**Biophysical Characterization of A$\beta$40 Assemblies.** Figure 1 shows negatively stained TEM images of A$\beta$40 at the four stages of self-assembly described above. From TEM images alone, one can not determine the abundance of aggregated A$\beta$40 species relative to A$\beta$40 monomers, especially in the early and intermediate stages of assembly. Four independent techniques were therefore used to characterize the distributions of A$\beta$40 species. First, PICUP experiments were performed, as previously introduced by Teplow and co-workers for studies of A$\beta$ self-assembly.[30a,b] The light exposure time and concentrations of cross-linking reagents were optimized to produce cross-linked oligomer bands in SDS-PAGE that differentiated among various stages of self-assembly (Figure S2). Results in Figures 2A,B with 0.5 s exposure times

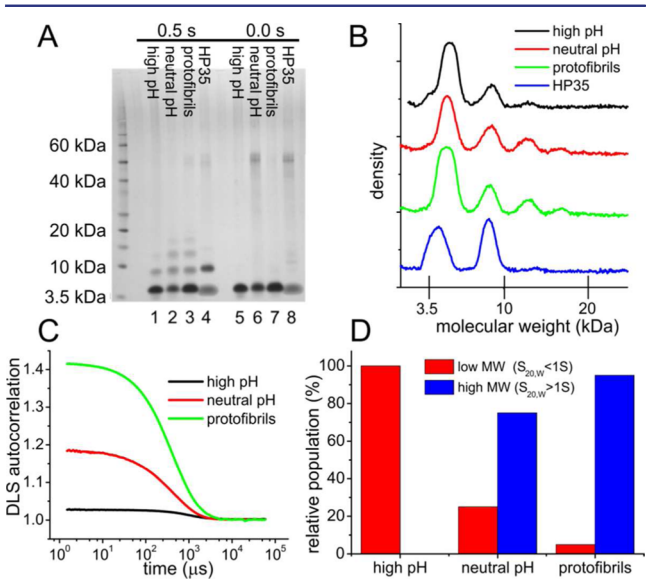


**Figure 2.** Biophysical characterization of A$\beta$40 assemblies. (A) SDS-PAGE gel of A$\beta$40 assemblies after PICUP cross-linking with 0.5 and 0.0 s light exposure times. A 2 mM solution of the 4.06 kDa protein HP35 in 50 mM phosphate buffer at pH 7.4 is used as a nonaggregating control. (B) Stain density profiles from lanes 1−4 of the SDS-PAGE gel. (C) DLS autocorrelation functions, with the amplitudes before 10 $\mu$s indicating the relative concentrations of large aggregates. (D) Populations of small (sedimentation coefficient $S_{20,w}$ < 1 S) and large ($S_{20,w}$ > 1 S) species determined by sedimentation velocity measurements. Here, $S_{20,w}$ represents the sedimentation coefficient normalized to the standard conditions of 20 °C and pure water solvent.

indicate negligible oligomer formation in the high-pH sample because the intensities of SDS-PAGE bands for cross-linked A$\beta$40 trimers and tetramers in the high-pH sample are no greater than those of the corresponding bands for the highly soluble protein HP35 that was used as a nonaggregating control. In contrast, neutral-pH and protofibril samples show larger trimer and tetramer bands. The dimer bands for HP35 and high-pH A$\beta$40 are attributable to cross-linking of monomers that collide in solution within the lifetime of free-radical species generated by the PICUP technique.

Second, DLS data in Figure 2C indicate a near absence of large A$\beta$40 assemblies in the high-pH sample and a higher concentration of large assemblies in the protofibril sample than in the neutral-pH sample. DLS measurements were performed within 2 min of initial preparation of the high-pH sample and


DOI: 10.1021/jacs.5b04843
J. Am. Chem. Soc. 2015, 137, 8294−8307

within 2 min of pH adjustment for the neutral-pH sample. In these measurements, large assemblies are defined to be those for which the DLS autocorrelation time is greater than 100 $\mu$s, corresponding roughly to particles with hydrodynamic radii greater than 10 nm. (Note that DLS measurements also indicated a monomeric state for HP35 at the 2 mM concentration used in the PICUP experiments.)

Third, sedimentation velocity measurements were performed on high-pH, neutral-pH, and protofibril samples. Results are summarized in Figure 2D. For each sample, absorption and interference data sets were analyzed in terms of a continuous distribution $c(s)$ of sedimenting species.[33] Data for the high-pH sample at 2.5 mM A$\beta$40 concentration (Figure S3A) indicate a single species with sedimentation coefficient $S_{20,w}$ = 0.37 S and estimated molar mass of 2.3 kDa. Because of the high peptide concentration, repulsive nonideality reduces the sedimentation coefficient and the apparent molar mass relative to the expected values for A$\beta$40 monomers. Data for the neutral-pH sample at 2.0 mM A$\beta$40 concentration (Figure S3B) indicate a distribution of aggregates, accounting for approximately 75% of the loading signal, with sedimentation coefficients broadly distributed around 11 S and estimated molar masses around 0.4 MDa. The remaining material is comprised of slowly sedimenting species near 0.6 S with an apparent molar mass of 4.7 kDa, close to the expected value of 4.3 kDa for monomeric A$\beta$40. Data for the protofibril sample at 2.0 mM A$\beta$40 concentration (Figure S3C) indicate that approximately 95% of the material consists of rapidly sedimenting species, with a broad distribution of sedimentation coefficients around 18 S and apparent molar masses of roughly 10 MDa. For comparison, a single protofibril with a molecular structure similar to that described by Qiang et al.[17c] for D23N-A$\beta$40 and with a length of 200 nm would have a molar mass of 1.8 MDa, suggesting that the major species observed in sedimentation velocity experiments are bundles of protofibrils.

For neutral-pH and protofibril samples, sedimentation velocity experiments were also performed on diluted samples (Figure S2D,E). The resulting data indicate dissolution of the large assemblies during these experiments, producing larger fractions of monomeric A$\beta$40 after dilution. From these data, it appears that the quasi-equilibrium solubilities of A$\beta$40 assemblies in the neutral-pH and protofibril samples are greater than 10 $\mu$M, consistent with low thermodynamic stability relative to mature fibrils, for which the quasi-equilibrium solubilities are typically less than 1 $\mu$M.[40]

On the basis of the TEM, PICUP, DLS, and sedimentation velocity measurements, we conclude that our high-pH A$\beta$40 samples are primarily (>90%) monomeric and that our neutral-pH samples are primarily (roughly 75%) oligomeric, with oligomerization numbers ranging from about 10 to more than 100. Our protofibril samples are primarily (>90%) protofibrillar assemblies.

High-pH, neutral-pH, and protofibril samples were also analyzed by SEC (Figure S4), but results from SEC are deemed unreliable because of interactions of A$\beta$40 with the SEC column material and dissolution of A$\beta$40 assemblies during chromatographic elution. For the high-pH sample, a single chromatographic peak was observed when the SEC column was equilibrated with 20 mM NaOH but at an apparent molecular weight of approximately 150 kDa. This observation is attributable to interaction of negatively charged A$\beta$40 molecules with the negatively charged agarose matrix of the column, which causes the protein to elute at an earlier volume.[41] Addition of 150 mM NaCl to the running buffer shifted the peak to a later value, corresponding to an apparent molecular weight of approximately 20 kDa. The discrepancy from the monomer value of 4.3 kDa may be attributable in part to the nonglobular structure of monomeric A$\beta$40.[42] SEC data for the neutral-pH sample also showed primarily a single peak at an elution volume similar to that observed for the high-pH sample. It should be noted that the width of this peak corresponds to a volume of roughly 1 mL, whereas the injected sample volume was 50 $\mu$L. Dilution of the neutral-pH sample during the SEC measurement may then reduce the apparent concentration of larger assemblies. SEC data for protofibrils show a broad distribution of assembly sizes, including a large fraction of material with apparent molecular weight greater than 1 MDa.

**Conformational Evolution of A$\beta$40 Probed by DNP-Enhanced ssNMR.** Structures of A$\beta$40 assemblies at the four stages described above were examined by ssNMR measurements on frozen solutions. As in previous DNP-enhanced ssNMR studies of biopolymers,[27−29] glycerol and paramagnetic dopants were added to produce glassy solutions amenable to DNP by the cross-effect mechanism.[26c,e] In experiments on high-pH and neutral-pH samples, glycerol and dopants were added immediately before loading the solutions into MAS rotors and immersing the rotors in liquid nitrogen. In experiments on protofibrils and fibrils, samples were pelleted by ultracentrifugation after addition of glycerol and paramagnetic dopants before these samples were frozen. CD measurements, shown in Figure 3, suggest that addition of glycerol may stabilize $\beta$-strand-like conformations of A$\beta$40 in

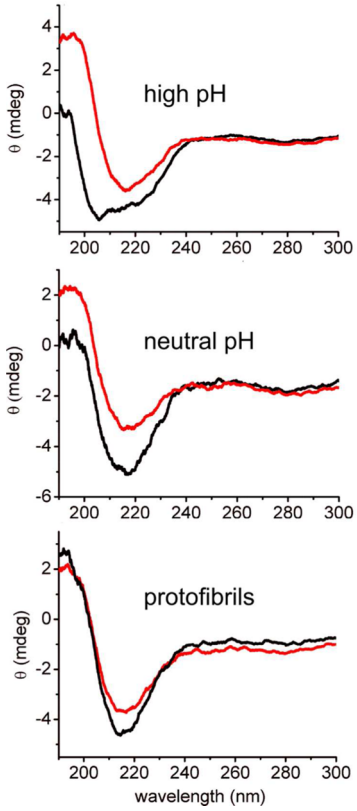


**Figure 3.** Circular dichroism spectra of high-pH, neutral-pH, and protofibril samples at 2.0 mM A$\beta$40 concentration (black spectra) and after mixing with an equal volume of glycerol (red spectra).


DOI: 10.1021/jacs.5b04843
J. Am. Chem. Soc. 2015, 137, 8294−8307

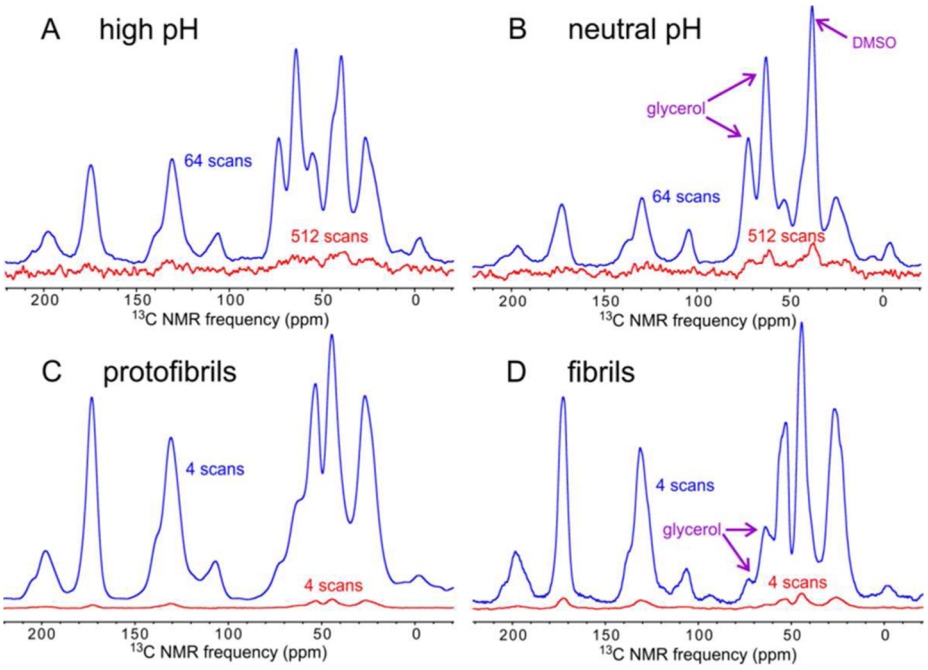


**Figure 4.** DNP enhancements of ssNMR signals from A$\beta$40 assemblies in frozen, triradical-doped glycerol/water solutions. (A–D) 1D, cross-polarized $^{13}$C spectra of high-pH, neutral-pH, fibril, and protofibril samples, respectively, prepared with isotopic-labeling pattern I (Table 1). Spectra were obtained at 100.8 MHz $^{13}$C NMR frequency, 25 K sample temperatures, and 6.7 kHz MAS frequency. Spectra with (blue) and without (red) microwave irradiation at 264.0 GHz are plotted on the same vertical scale in each panel and with the indicated number of scans for each spectrum. DNP enhancement factors, defined as the ratio of signal amplitudes with and without microwave irradiation, are 80, 60, 32, and 18 in panels A–D, respectively. Recycle delays are 5.6, 5.0, 25.0, and 30.0 s.

high-pH and neutral-pH samples. The metastability of protofibrils[8a,17c] and stability of fibrils implies that structural changes during ultracentrifugation were negligible. Samples were subsequently kept below 100 K at all times.

Figure 4 compares 1D, cross-polarized $^{13}$C NMR spectra of high-pH, neutral-pH, protofibril, and fibril samples in the frozen glycerol/water solutions with and without microwave irradiation at sample temperatures near 25 K and with 6.7 kHz MAS. DNP signal enhancement factors in these spectra are in the 18–80 range. Without these DNP enhancements, the ssNMR measurements described below would have been prohibitively time-consuming.

DNP enhancement factors for protofibril and fibril samples are lower than those for high-pH and neutral-pH samples. We attribute this observation in part to binding of triradical dopants to the protofibrils and fibrils, producing high local concentrations of dopants that render DNP less effective. As discussed above, nominal dopant concentrations in protofibril and fibril samples were deliberately lower than in high-pH and neutral-pH samples. Higher dopant concentrations were found to produce lower enhancement factors for protofibrils and fibrils. Enhancement factors for protofibrils and fibrils are also reduced by the higher density of A$\beta$40 assemblies in these samples, which reduces the local $^{1}$H spin–lattice relaxation times.

Figure 5 shows 2D $^{13}$C–$^{13}$C NMR spectra of A$\beta$40 samples with isotopic-labeling pattern I (Table 1), obtained with 23.8 ms spin diffusion mixing periods. $^{13}$C NMR lines for uniformly $^{15}$N,$^{13}$C-labeled residues F19 and L34 are quite broad in high-pH and neutral-pH samples (4.4–7.4 ppm full width at half-maximum, fwhm), are somewhat sharper in protofibrils (3.0–5.2 ppm fwhm), and are sharpest in fibrils (2.4–3.2 ppm fwhm). This progression (Figure 6) indicates an increasing degree of conformational order. Although $^{13}$C ssNMR line widths in the 2.4–3.2 ppm range are still large compared with line widths in ssNMR spectra of well-structured, hydrated proteins near room temperature, $^{13}$C ssNMR line widths of well-structured peptides and proteins in frozen glycerol/water solutions are commonly 2 ppm or greater.[24,26d] $^{13}$C ssNMR line widths in Figure 5 are not determined by transverse spin relaxation rates (see Table S1).

Average $^{13}C_{\alpha}$ and $^{13}C_{\beta}$ chemical shifts (i.e., chemical shifts at crosspeak maxima) for L34 are similar in protofibril and fibril samples (vertical blue dashed lines in Figure 5). For F19, $^{13}C_{\alpha}$ chemical shifts of protofibril and fibril samples are significantly different (green dashed line), but $^{13}C_{\beta}$ chemical shifts are similar (red dashed line). $^{13}$C chemical shifts for F19, L34, and G38 are summarized in Figure 6. $^{13}C_{\alpha}$ and $^{13}$CO secondary shifts (i.e., differences from random coil values[43]) are negative, and $^{13}C_{\beta}$ secondary shifts are positive for both F19 and L34 in protofibril and fibril samples, indicating $\beta$-strand-like conformations at these residues.[44] $^{13}$CO secondary shifts for G38 are negative, also indicating a $\beta$-strand-like conformation. Average $^{13}C_{\alpha}$ secondary shifts for G38 in protofibril and fibril samples are similar but can not be interpreted in terms of conformational preference because $^{13}C_{\alpha}$ secondary shifts for glycine residues in proteins do not correlate strongly with secondary structure.

Average $^{13}$C secondary shifts in neutral-pH and high-pH samples exhibit the same patterns (except for $^{13}$CO of F19), indicating a predominance of extended, $\beta$-strand-like conformations despite the greater conformational disorder in these samples. For comparison, $^{13}$C secondary shifts in a 2D $^{13}$C–$^{13}$C NMR spectrum of a lyophilized A$\beta$40 powder after HFIP treatment, recorded at room temperature, are quite different and are consistent with predominant $\alpha$-helical conformations at F19 and L34 (Figure S5).


DOI: 10.1021/jacs.5b04843
J. Am. Chem. Soc. 2015, 137, 8294–8307

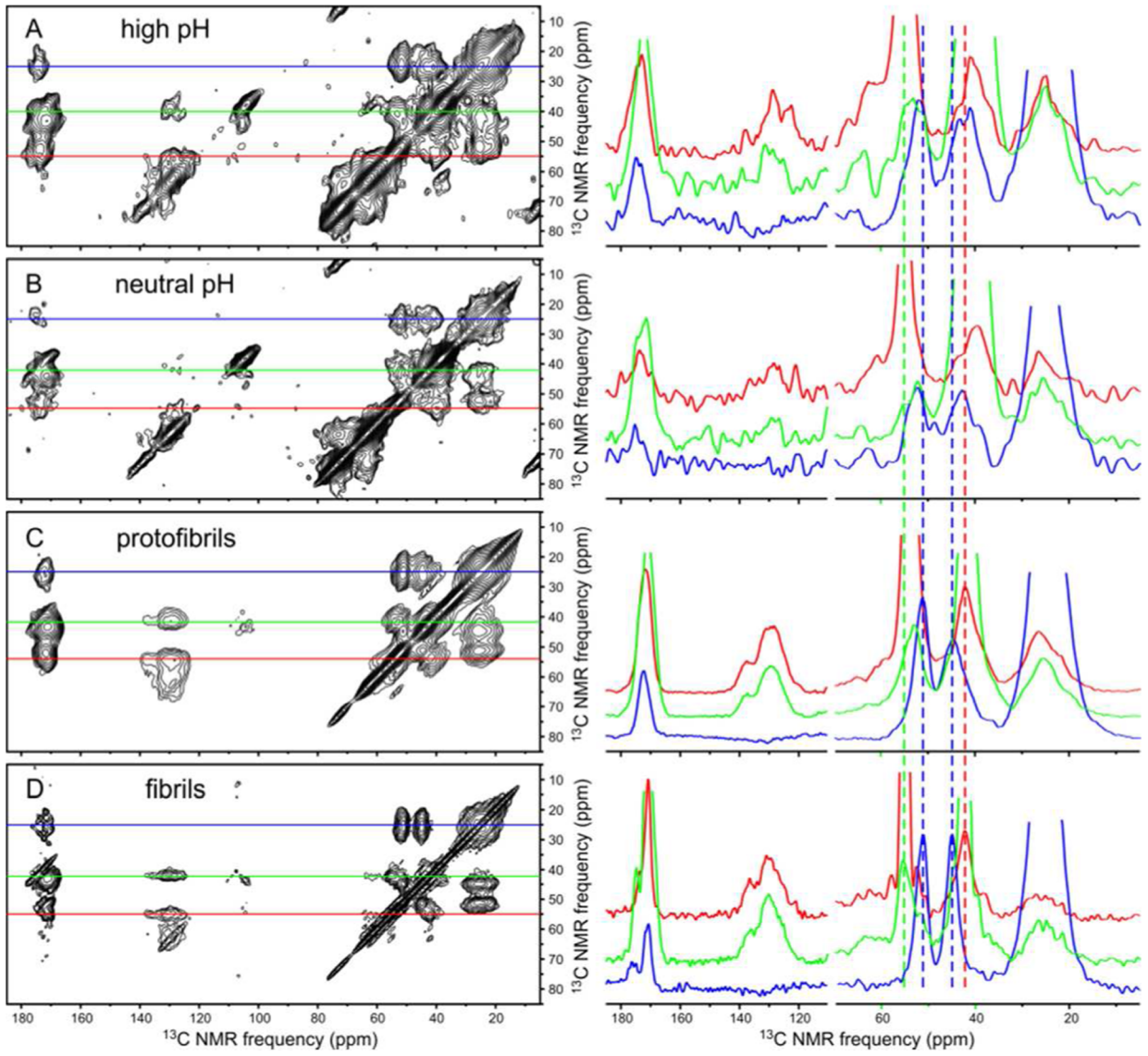


**Figure 5.** DNP-enhanced 2D $^{13}$C ssNMR spectra of A$\beta$40 assemblies with isotopic-labeling pattern I. (A) High-pH sample, acquired with 5.6 s recycle delay, 2.7 ms maximum $t_1$ period, total measurement time of 5.0 h, processed with 150 Hz Gaussian apodization in both dimensions. (B) Neutral-pH sample, acquired with 5.7 s recycle delay, 2.7 ms maximum $t_1$ period, total measurement time of 5.0 h, and 150 Hz Gaussian apodization. (C) Protofibril sample, acquired with 10.0 s recycle delay, 3.9 ms maximum $t_1$ period, total measurement time of 1.5 h, and 50 Hz Gaussian apodization. (D) Fibril sample, acquired with 10.2 s recycle delay, 3.9 ms maximum $t_1$ period, total measurement time of 1.7 h, and 50 Hz Gaussian apodization. 1D slices at $^{13}$C chemical shifts of L34 $C_\gamma$ (blue), F19 $C_\beta$ (green), and F19 $C_\alpha$ (red) are shown to the right of each 2D spectrum. Vertical dashed lines indicate peak positions in the fibril spectrum. Samples were in frozen glycerol/water at 25 K with triradical dopants. Spectra were acquired with 6.7 kHz MAS and 23.8 ms spin-diffusion mixing periods between $t_1$ and $t_2$ periods. Contour levels increase by successive factors of 1.3.

DNP-enhanced 2D $^{15}$N−$^{13}$C NMR spectra of high-pH, neutral-pH, protofibril, and fibril samples were also acquired (Figure S6). The reduced disorder in A$\beta$40 fibrils relative to the other samples is also apparent in these spectra.

Additional information about the A$\beta$40 conformation comes from the 2D $^{13}$C−$^{13}$C NMR spectra in Figure 7, which were obtained with 2.1 s RAD mixing periods. The spectrum of the fibril sample (Figure 7D) shows a strong crosspeak between L34 methyl signals (near 25 ppm) and F19 aromatic signals (near 130 ppm), indicating proximity of L34 and F19 side chains. This crosspeak is expected in the fibril sample spectrum because previously reported structural models for A$\beta$40 fibrils include F19−L34 contacts within double-layered, parallel cross-$\beta$ motifs, as depicted in Figure 8A. Surprisingly, F19−L34 crosspeaks are also observed in 2D RAD spectra of high-pH and neutral-pH samples (Figure 7A,B), suggesting that F19−L34 contacts are present even before structurally ordered assemblies develop. The F19−L34 crosspeak in the 2D RAD spectrum of the protofibril sample (Figure 7C) is even more intense than in the spectrum of the fibril sample, suggesting a shorter distance between F19 and L34 side chains in the protofibrils and providing an initial indication that the protofibril structure may be significantly different from the fibril structure (see below). F19−L34 crosspeak volumes, normalized to intraresidue L34 crosspeaks in the same spectra, are quantified in Figure 8B.

Liquid-state NMR studies of full-length A$\beta$ peptides in aqueous solution near neutral pH and at 4−10 °C have shown


DOI: 10.1021/jacs.5b04843
J. Am. Chem. Soc. 2015, 137, 8294−8307

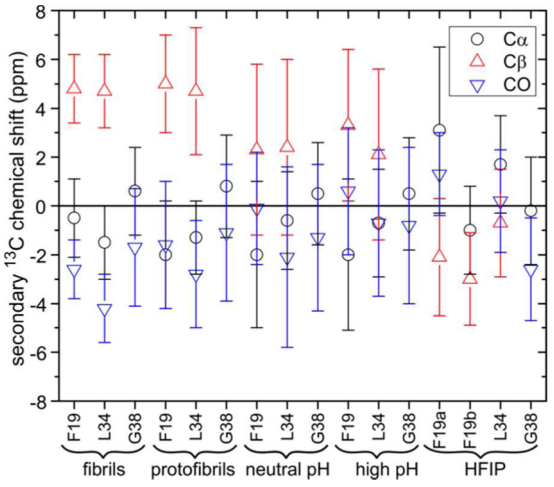


**Figure 6.** Secondary chemical shifts for carbonyl, $C_\alpha$, and $C_\beta$ sites in F19, L34, and G38, relative to random coil shifts reported by Wishart et al.[43] Error bars indicate the full widths at half maxima measured from crosspeaks in 2D ssNMR spectra of the A$\beta$40 samples. In addition to data from DNP-enhanced spectra of high-pH, neutral-pH, protofibril, and fibril samples in frozen solutions, data are also shown for an A$\beta$40 powder prepared by lyophilization of an HFIP solution.

that these peptides are largely unstructured in the unassembled state,[42] with partial population of $\beta$-strand conformations in certain segments, including segments that contain F19 and L34.[42b] In our experiments, the primarily monomeric state is prepared at pH 12 and higher A$\beta$40 concentrations, and glycerol is added prior to freezing. The freezing process occurs within several seconds, allowing conformational changes until the solvent approaches its glass-transition temperature. These differences in sample preparation may produce differences in conformational distributions observed by liquid-state NMR and ssNMR.

**Supramolecular Structure in A$\beta$40 Protofibrils and Fibrils.** A$\beta$40 fibrils have been shown to contain cross-$\beta$ structures comprised of in-register parallel $\beta$ sheets, meaning that identical residues of neighboring molecules align with one another within the $\beta$ sheets (through intermolecular hydrogen bonds between backbone amide and carbonyl groups of residue $k$ in one $\beta$ strand and carbonyl and amide groups of residues $k - 1$ and $k + 1$ in a neighboring $\beta$ strand). Less is known about supramolecular structures in protofibrils. A double-layered antiparallel $\beta$-sheet structure has been identified in protofibrils formed by D23N-A$\beta$40 under the specific conditions described by Qiang et al.[17c] In these D23N-A$\beta$40 protofibrils, residues 17−21 form an antiparallel $\beta$ sheet with interstrand hydrogen bonds between residue 19+$k$ and residue 19−$k$, whereas residues 30−36 form an antiparallel $\beta$ sheet with interstrand hydrogen bonds between residue 33+$k$ and 33−$k$. It is not known whether the same antiparallel supramolecular structure exists in wild-type A$\beta$40. As one alternative, it has been suggested that A$\beta$ protofibrils may contain $\beta$-sheet structures comprised of $\beta$ hairpins in which the $\beta$ sheets would involve both intermolecular and intramolecular hydrogen bonds among two separate $\beta$-strand segments in the A$\beta$ sequence.[23,45] It should be emphasized that no intramolecular hydrogen bonds are present in existing ssNMR-based models for wild-type or mutant A$\beta$ fibrils or D23N-A$\beta$40 protofibrils[5a,15a−c,e,f,17c,46] and that these models do not contain true $\beta$ hairpins.

The rf pulse sequence in Figure 9A was used to measure intermolecular $^{13}$C spin polarization transfers between labeled carbonyl and aliphatic sites, which depend on intermolecular $^{13}$C−$^{13}$C distances and hence on supramolecular structure. In this pulse sequence, longitudinal $^{13}$C polarization was first created by $^{1}$H−$^{13}$C cross-polarization, a $^{13}$C "flip-back" pulse, and a period $\tau_z$ for dephasing of transverse polarization. A weak Gaussian-shaped $\pi$ pulse at the carbonyl $^{13}$C NMR frequency was then either present or absent on successive free-induction decay (FID) acquisitions, effectively allowing carbonyl $^{13}$C polarization to be prepared selectively by taking the difference between successive FIDs. Carbonyl polarization was then allowed to transfer to other $^{13}$C sites during the polarization transfer period $\tau_{pt}$. Values of $\tau_{pt}$ ranged from 0.6 ms to 4.0 s.

Alternative ssNMR methods for characterizing supramolecular structure in A$\beta$ assemblies, such as the dipolar recoupling techniques used in previous studies of selectively labeled amyloid fibrils,[5a,15b,16a,25a,47] were also considered but were ruled out by the relatively short transverse spin relaxation times in paramagnetically doped frozen solutions (Table S1) and the relatively low MAS frequencies that are achievable at low temperatures. It should also be noted that methyl group rotation is fully quenched near 25 K so that (unlike the typical situation at temperatures above 100−150 K) methyl $^{13}$C labels have $^{1}$H−$^{13}$C dipole−dipole couplings even stronger than those of methylene $^{13}$C labels.

As a test of the pulse sequence in Figure 9A under low-temperature DNP conditions, measurements were performed on a sample of fibrils formed by a peptide comprised of residues 11−25 of A$\beta$ (A$\beta_{11-25}$) synthesized with $^{13}$C labels at the carbonyl site of F20 and the $C_\beta$ site of A21. A$\beta_{11-25}$ fibrils have been the subject of previous structural studies by ssNMR, which show that F20 and A21 are contained in a $\beta$-strand segment,[25a] implying an intramolecular distance between carbonyl and $C_\beta$ labels of 3.4 ± 0.2 Å. For these measurements, A$\beta_{11-25}$ fibrils (approximately 5 mg) were suspended in the same glycerol/water solvent as in measurements on A$\beta$40 assemblies, with 1 mM DOTOPA-3OH-Methoxy. Data in Figure S7 show a buildup of $C_\beta$ NMR signals in difference spectra with increasing $\tau_{pt}$ on the 425 ms time scale, with a maximum polarization transfer of approximately 40%.

Measurements to probe supramolecular structure in A$\beta$40 fibrils and protofibrils were performed on samples II−IV (Table 1), in which assemblies were formed from mixtures of molecules with single $^{13}$C labels at carbonyl and aliphatic sites. To ensure random mixtures within the assemblies, carbonyl-labeled and aliphatic-labeled molecules were synthesized and purified simultaneously as described in the Methods section. Figure 9B shows examples of $^{13}$C NMR difference spectra for protofibrils and fibrils prepared from A$\beta$40 sample III. With $\tau_{pt}$ = 3 ms, the difference spectra show strong carbonyl lines from the $^{13}$C-labeled A30 carbonyl site and natural-abundance carbonyl $^{13}$C sites (near 177 ppm) as well as weaker signals from glycerol (near 65 ppm) and MAS sidebands of carbonyl and glycerol signals (near 199, 132, 110, and 43 ppm). As $\tau_{pt}$ increases, signals from $^{13}$C-labeled A30 $C_\beta$ sites (near 25 ppm) increase primarily because of intermolecular polarization transfers from $^{13}$C-labeled A30 carbonyl sites.

Difference spectra for all A$\beta$40 samples are shown in Figure S8. Figure 9C shows the dependences of A21 and A30 $C_\beta$ signal areas (for A$\beta$40 samples II and III) and G33 $C_\alpha$ signal areas (for A$\beta$40 sample IV) on $\tau_{pt}$. The normalized signal areas are calculated from the expression $a_{meth}/(a_{carb} + a_{meth})$, where $a_{meth}$


DOI: 10.1021/jacs.5b04843
J. Am. Chem. Soc. 2015, 137, 8294−8307

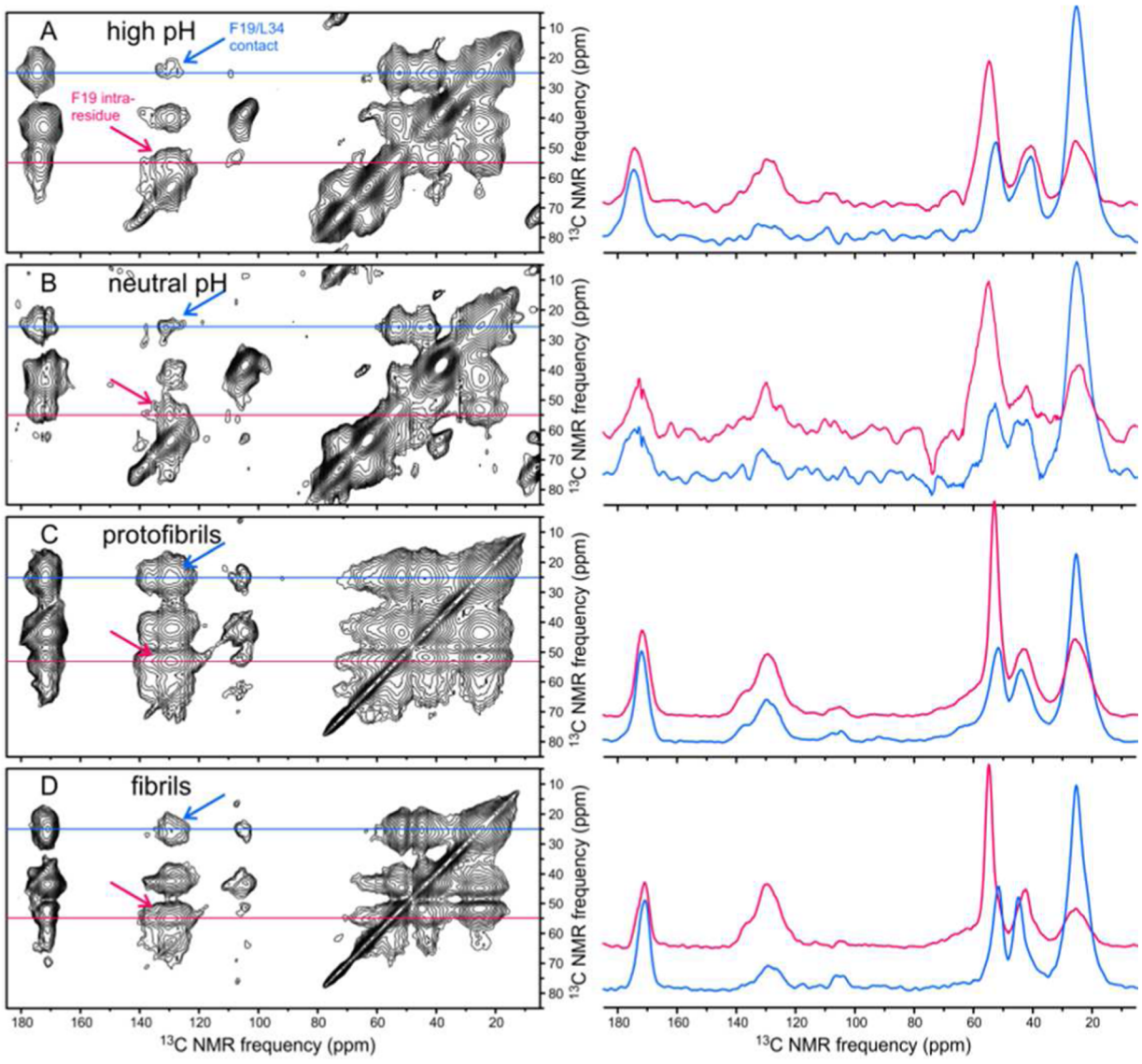


**Figure 7.** DNP-enhanced 2D $^{13}$C ssNMR spectra of A$\beta$40 assemblies, obtained with 2.1 s RAD mixing periods. (A–D) Spectra of high-pH, neutral-pH, protofibril, and fibril samples, respectively, with 1D slices at $^{13}$C chemical shifts of L34 C$_\gamma$ (red) and F19 C$_\alpha$ (blue) shown to the right of each 2D spectrum. Samples were prepared with isotopic-labeling pattern I. Sample temperatures, MAS frequencies, maximum $t_1$ periods, and recycle delays were the same as in Figure 4. Total measurement times were 5.0, 5.0, 1.7, and 3.0 h, respectively. Gaussian apodizations were 250, 250, 150, and 150 Hz, respectively. Blue arrows indicate interresidue crosspeaks between F19 aromatic and L34 aliphatic signals. Red arrows indicate crosspeaks between F19 aromatic and F19 C$_\alpha$ signals.

and $a_{carb}$ are C$_\beta$ (or C$_\alpha$) and carbonyl signal areas in the difference spectra so that the plots in Figure 9C represent fractional polarization transfers. Data are shown for protofibrils and fibrils, prepared as described above, and also for fibrils that were grown from preformed A$\beta$40 fibril seeds with the threefold-symmetric molecular structures reported previously by Paravastu et al.[15b] (cyan symbols in Figure 9C). In all cases, the data can be fit with double-exponential functions (solid lines in Figure 9C) of the form $S(\tau_{pt}) = (S_1 + S_2) - S_1 \exp(-\tau_{pt}/\tau_1) - S_2 \exp(-\tau_{pt}/\tau_2)$. Values of the best-fit parameters are given in Table 2.

We attribute the rapidly increasing signal components (parameters $S_1$ and $\tau_1$) to intramolecular polarization transfers from carbonyl $^{13}$C labels or natural-abundance carbonyl $^{13}$C to natural-abundance aliphatic $^{13}$C and from natural-abundance carbonyl $^{13}$C to aliphatic $^{13}$C labels. We attribute the slowly increasing signal components (parameters $S_2$ and $\tau_2$) to intermolecular polarization transfers from carbonyl $^{13}$C labels. For all fibril samples, $S_2 \approx 0.12 \pm 0.03$. For fibrils prepared from A$\beta$40 samples II and III, $\tau_2 \approx 3 \pm 1$ s. The similar values of these parameters for different fibril samples indicates similar intermolecular carbonyl–C$_\beta$ distances for A21 and A30, as expected in an in-register parallel $\beta$-sheet structure. For fibrils prepared from A$\beta$40 sample IV, $\tau_2 \approx 1.2 \pm 0.2$ s. This smaller value of $\tau_2$ is also expected because the nearest-neighbor intermolecular carbonyl–C$_\alpha$ distance for G33 is expected to be less than the nearest-neighbor intermolecular carbonyl–C$_\beta$ distances for A21 and A30. In an ideal in-register parallel $\beta$ sheet, these distances would be approximately 4.2 Å for G33 and 4.5 Å for A21 and A30, which would imply a ratio of approximately 1.5 for the polarization transfer rates in the crude approximation that these rates are strictly proportional to $R^{-6}$, with $R$ being the nearest-neighbor distance between carbonyl and aliphatic $^{13}$C labels.


DOI: 10.1021/jacs.5b04843
J. Am. Chem. Soc. 2015, 137, 8294–8307

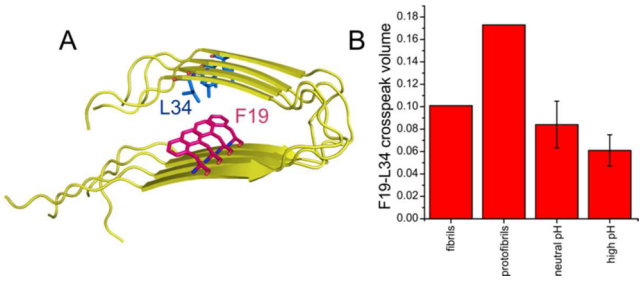


**Figure 8.** (A) Cartoon representation of a cross-$\beta$ structural motif in A$\beta$40 fibrils, adapted from Protein Databank file 2LMP, showing the proximity of F19 and L34 side chains in the core of the double-layered parallel $\beta$-sheet structure that is known to exist in A$\beta$40 fibrils. (B) Interresidue F19−-L34 crosspeak volumes from 2D $^{13}$C ssNMR spectra in Figure 5, normalized to the sum of intraresidue L34 CO−$C_\gamma$, $C_\alpha$−$C_\gamma$, and $C_\beta$−$C_\gamma$ crosspeak volumes in the same spectra. Error bars for neutral-pH and high-pH data represent uncertainty caused by the root-mean-squared noise in the experimental spectra. Uncertainties for fibril and protofibril data are at least five times smaller.

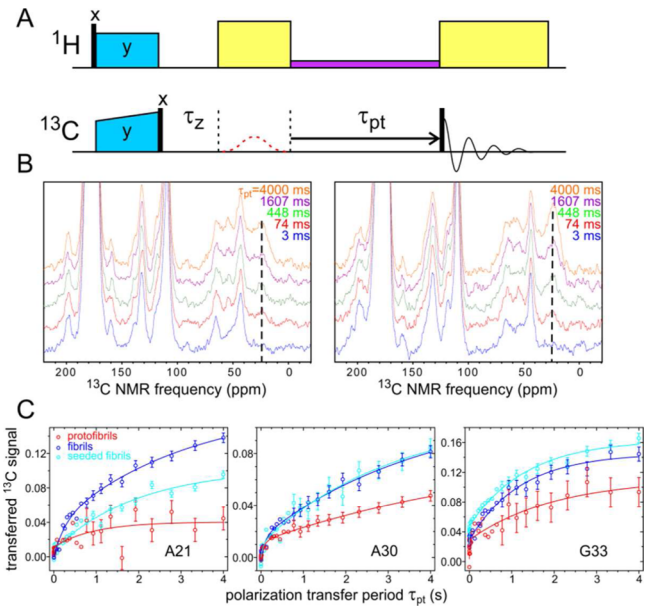


**Figure 9.** Characterization of supramolecular structures in A$\beta$40 protofibrils and fibrils by measurements of intermolecular $^{13}$C spin polarization transfers. (A) Radio frequency pulse sequence for polarization transfer experiments, showing $^1$H−$^{13}$C cross-polarization (blue period), a 3 ms "z-filter" dephasing period $\tau_z$, a 0.6 ms Gaussian-shaped frequency-selective $\pi$ pulse applied to carbonyl $^{13}$C sites on alternating signal acquisitions (dashed red line), the incremented polarization-transfer period $\tau_{pt}$ with RAD irradiation (purple), and signal acquisition after a $^{13}$C $\pi/2$ pulse (black bars). Yellow blocks indicate $^1$H decoupling. (B) Examples of $^{13}$C difference spectra (with and without the frequency-selective $\pi$ pulse) for A$\beta$40 protofibrils (left) and fibrils (right) with isotopic-labeling pattern III, showing the growth of A30 $C_\beta$ signals with increasing $\tau_{pt}$ (dotted lines). (C) Polarization-transfer curves for fibrils and protofibrils with isotopic-labeling patterns II, III, and IV, showing the growth of signals from A21 $C_\beta$, A30 $C_\beta$, and G33 $C_\alpha$ sites caused by polarization transfers from A21, A30, and G33 carbonyl sites, respectively. For each curve, $C_\beta$ or $C_\alpha$ signals in difference spectra, integrated over 7−10 ppm intervals, are normalized to integrated carbonyl signals in the same spectra. Solid lines are least-squares fits with a double exponential function as described in the text. Seeded fibrils were grown by using as seeds sonicated fragments of A$\beta$40 fibrils with the threefold symmetric structure described by Paravastu et al.[15b].

Polarization transfer data for A$\beta$40 fibrils are also consistent with the results for A$\beta_{11-25}$ fibrils described above and shown in Figure S7. Assuming polarization transfer rates to be proportional to $R^{-6}$, values of $\tau_2$ for A$\beta$40 fibrils should be about 5.4 times (for samples II and III) or 3.6 times (for sample IV) greater than the value of $\tau_2$ for A$\beta_{11-25}$ fibrils. Results in Table 2 are in reasonable agreement with this crude prediction.

The observation that $S_2$ for A$\beta_{11-25}$ fibrils is roughly 3−4 times larger than $S_2$ for A$\beta$40 fibrils is attributable to the larger contribution of natural-abundance $^{13}$C to the total carbonyl NMR signal area in difference spectra of A$\beta$40 fibrils and to the fact that the A$\beta$40 fibrils are comprised of mixtures of carbonyl- and aliphatic-labeled molecules. Natural-abundance $^{13}$C accounts for approximately 50% of the total carbonyl signal area $a_{carb}$ in the A$\beta$40 fibril samples but only 17% in the A$\beta_{11-25}$ fibrils. In addition, only about 50% of carbonyl-labeled A$\beta$40 molecules have an aliphatic-labeled nearest neighbor.

For all A$\beta$40 protofibrils, the polarization transfer data in Figure 9C are fit with smaller and more variable values of $S_2$ (0.02−0.10) and with more variable values of $\tau_2$ (0.1−10 s) compared with data for A$\beta$40 fibrils. The smaller polarization transfer amplitudes for A$\beta$40 protofibrils indicate longer intermolecular carbonyl−aliphatic distances for the labeled sites in protofibrils than in fibrils. Data for protofibrils prepared from A$\beta$40 sample II show very little polarization transfer, indicating nearest-neighbor intermolecular carbonyl−$C_\beta$ distances for A21 that greatly exceed 5 Å. Thus, these data support the absence of in-register parallel $\beta$-sheet structures in wild-type A$\beta$40 protofibrils.

In the structural model for D23N-A$\beta$40 protofibrils developed by Qiang et al.[17c] (Protein Data Bank file 2LNQ), nearest-neighbor intemolecular distances between G33 carbonyl and G33 $C_\alpha$ sites are 5.0 ± 0.2 Å, whereas nearest-neighbor intermolecular distances between A30 carbonyl and A30 $C_\beta$ sites or between A21 carbonyl and A21 $C_\beta$ sites are greater than 9 Å. If the same double-layered antiparallel $\beta$-sheet structure exists in wild-type A$\beta$40 fibrils, then one would expect the time scale for polarization transfer in protofibrils prepared from A$\beta$40 sample IV to be roughly three times greater than that of fibrils prepared from A$\beta$40 sample IV, and the time scale for polarization transfer in protofibrils prepared from A$\beta$40 samples II and III to be more than 10 times greater than that of the corresponding fibrils. Data in Figure 9 do not agree completely with these expectations, particularly in the case of A$\beta$40 sample III. Therefore, our data do not prove that wild-type A$\beta$40 protofibrils have the same supramolecular structure as D23N-A$\beta$40 protofibrils.

## DISCUSSION

**Summary of Conclusions from DNP-Enhanced ssNMR Data.** Experiments described above provide new information about the structural properties of intermediates in the A$\beta$40 assembly process. First, it is clear from the $^{13}$C NMR line widths in Figures 5 and 6 that the degree of conformational order increases progressively as assembly proceeds from the largely monomeric state prepared initially at high pH, to the largely oligomeric state that develops quickly after pH neutralization, to the metastable protofibrillar state that subsequently develops over a period of several hours, and finally to the mature fibrillar state that is produced by several rounds of sonication and incubation. Remarkably, the predominant molecular conformations are similar at all stages. In particular, average $^{13}$C secondary chemical shifts for


DOI: 10.1021/jacs.5b04843
J. Am. Chem. Soc. 2015, 137, 8294−8307

**Table 2. Best-Fit Parameters for Polarization Transfer Data in Figures 7, S8, and S9**

| peptide sample | assembly type | $S_1$ | $S_2$ | $\tau_1$ (ms) | $\tau_2$ (ms) |
|---|---|---|---|---|---|
| A$\beta$40 II | protofibrils | 0.011 ± 0.005 | 0.029 ± 0.008 | 2.6 ± 4.6 | 950 ± 700 |
| | fibrils | 0.036 ± 0.014 | 0.140 ± 0.024 | 250 ± 110 | 3100 ± 1600 |
| | seeded fibrils | 0.008 ± 0.003 | 0.095 ± 0.009 | 5.6 ± 6.9 | 2000 ± 440 |
| A$\beta$40 III | protofibrils | 0.012 ± 0.001 | 0.074 ± 0.032 | 77 ± 23 | 6200 ± 3800 |
| | fibrils | 0.015 ± 0.003 | 0.101 ± 0.018 | 102 ± 41 | 3800 ± 1300 |
| | seeded fibrils | 0.010 ± 0.004 | 0.099 ± 0.022 | 61 ± 59 | 3200 ± 1300 |
| A$\beta$40 IV | protofibrils | 0.029 ± 0.004 | 0.082 ± 0.0.018 | 4.4 ± 2.9 | 2000 ± 990 |
| | fibrils | 0.029 ± 0.002 | 0.116 ± 0.005 | 0.3 ± 0.2 | 1210 ± 140 |
| | seeded fibrils | 0.048 ± 0.002 | 0.116 ± 0.004 | 0.9 ± 0.2 | 1330 ± 130 |
| $A\beta_{11-25}$ | fibrils | 0.014 ± 0.003 | 0.392 ± 0.006 | 0.1 ± 0.7 | 425 ± 20 |

carbonyl, $C_\alpha$, and $C_\beta$ sites of F19, L34, and G38 indicate extended, $\beta$-sheet-like conformations in ssNMR spectra of high-pH, neutral-pH, protofibril, and fibril samples. Absolute values of secondary shifts for carbonyl sites are somewhat reduced in neutral-pH and high-pH samples, consistent with the absence of ordered $\beta$-sheet structures prior to the formation of protofibrils.

In addition, F19−L34 side chain contacts are evident in the 2D spectra in Figure 7, indicating that A$\beta$40 conformations similar to the U-shaped conformation in mature fibrils (Figure 8A) are highly populated at all stages, even before formation of ordered $\beta$ sheets and before formation of oligomers that are large enough to be visible in TEM images. Thus, the predominant molecular conformation can be considered to be independent of the supramolecular structure in A$\beta$40 assemblies. In principle, disruption of this conformation might simultaneously prevent the formation of oligomers, protofibrils, and fibrils.

Protofibrils form within several hours but then persist for at least 20 days at room temperature in the absence of sonication or agitation of the A$\beta$40 solution. Conversion to fibrils is accelerated by periodic sonication. This observation can be explained by the existence of a small population of fibrils that develops spontaneously from monomers or small oligomers, possibly during the same period when the majority of A$\beta$40 molecules are self-assembling into protofibrils. Sonication breaks the fibrils and protofibrils into shorter fragments, creating more fibril and protofibril ends and thereby accelerating the transfer of A$\beta$40 molecules from the less thermodynamically stable protofibrils to the more stable fibrils. This transfer presumably occurs by gradual dissolution of the less stable structures and extension of the more stable structures, as discussed by Qiang et al.[40a] Under the conditions of our experiments, nucleation of protofibril structures is apparently more rapid than nucleation of fibril structures, accounting for the much greater abundance of protofibrils than fibrils prior to sonication.

The metastability of protofibrils suggests that their molecular structures must be significantly different from those of fibrils so that conversion of protofibrils to fibrils can not occur by internal structural rearrangements. In other words, protofibrils are "off-pathway" intermediates and are not simply defective fibrils. $^{13}C$ spin polarization transfer data in Figure 9 indicate a significant difference in supramolecular organization, implying that protofibril-to-fibril conversion requires a rearrangement of the hydrogen-bonding patterns within $\beta$ sheets, which can not occur at an appreciable rate within an intact assembly. Data in Figure 9 show that the in-register, parallel $\beta$-sheet structure of mature A$\beta$40 fibrils does not exist within A$\beta$40 protofibrils. Polarization transfer curves for protofibrils in Figure 9C are consistent with antiparallel $\beta$ sheets, but the precise intermolecular alignment in the protofibrils can not be determined from these data.

It should be noted that the A$\beta$40 concentration and solvent composition in our experiments are quite different from those in physiological settings, as are many other factors. Therefore, the stages of A$\beta$40 self-assembly examined in our experiments are not necessarily relevant to the physiological self-assembly process.

**Comparisons with Previous Studies of A$\beta$ Self-Assembly Intermediates.** The first ssNMR studies of A$\beta$ self-assembly intermediates were reported by Ishii and co-workers,[7c,d] who studied large (~650 kDa), long-lived, spherical A$\beta$40 assemblies that form at 4 °C, pH 7.4, and 100 $\mu$M peptide concentration. $^{13}C$ chemical shifts were found to be quite similar in lyophilized spherical assemblies and in A$\beta$40 fibrils, consistent with our data for smaller A$\beta$40 oligomers with shorter lifetimes. Measurements of intermolecular $^{13}C-^{13}C$ dipole−dipole couplings indicated a predominantly parallel intermolecular alignment in the large spherical assemblies,[7d] in contrast to our results. TEM images reported by Ishii and co-workers suggest a direct evolution of their spherical assemblies to mature fibrils after more than 50 h of incubation, without the development of a large population of metastable protofibrils and without sonication or agitation of the A$\beta$40 solution. Thus, it appears that the preference for parallel intermolecular alignment within large, spherical A$\beta$40 assemblies, under the conditions employed by Ishii and co-workers, may permit an "on-pathway" conversion of the spherical assemblies to fibrillar assemblies by internal structural rearrangements, without the dissolution discussed above. More recently, Ishii and co-workers have reported ssNMR studies of spherical A$\beta$42 assemblies, called "amylospheroids", which they also found to contain predominantly parallel intermolecular alignments and molecular conformations similar to the A$\beta$40 conformation depicted in Figure 8A.[18b]

Paravastu and co-workers performed ssNMR studies of small, metastable A$\beta$42 oligomers, prepared by dialysis from 100 $\mu$M peptide solutions that contain SDS.[7b] Again, $^{13}C$ chemical shifts indicated similar molecular conformations in A$\beta$42 oligomers and A$\beta$42 fibrils, which were prepared separately without SDS. Measurements of intermolecular $^{13}C-^{13}C$ dipole−dipole couplings indicated the absence of in-register, parallel alignment in the oligomers, although short intermolecular distances between V36 carbonyl sites were detected. Consistent with our results for A$\beta$40 self-assembly intermediates, differences in $\beta$-sheet structure appear to account for the metastability and off-pathway nature of these A$\beta$42 oligomers.


DOI: 10.1021/jacs.5b04843
J. Am. Chem. Soc. 2015, 137, 8294−8307

Smith and co-workers[20] performed studies of small A$\beta$42 oligomers (formed at 200 $\mu$M peptide concentration) that were metastable at 4 °C but converted within 6 h to protofibrils at 37 °C and then to fibrils within 12 days. From a combination of ssNMR, atomic force microscopy, and other measurements, they concluded that these oligomers were pentameric or hexameric discs, in which the A$\beta$42 conformation was similar to that in A$\beta$42 fibrils but which lacked $\beta$ sheet organization.

Huster and co-workers performed ssNMR studies of A$\beta$40 protofibrils (formed at 900 $\mu$M peptide concentration) that were stabilized by interactions with the antibody B10AP.[19] Again, their $^{13}$C chemical shift data indicate similar conformations in protofibrils and fibrils. Additionally, they observed long-range $^{13}$C−$^{13}$C crosspeak signals between E22 and I31 in 2D ssNMR spectra of B10AP-stabilized protofibrils that are absent from spectra of A$\beta$40 fibrils, an observation that they interpret as evidence for a significant difference in $\beta$-sheet structure.

Reif and co-workers[21] performed ssNMR studies of small A$\beta$40 oligomers (formed at 100 $\mu$M peptide concentration) that were stabilized by interactions with EGCG, a compound from green tea that is reported to render the oligomers nontoxic. Their data indicate a longer disordered N-terminal tail in EGCG-stabilized oligomers than in A$\beta$40 fibrils but otherwise a similar molecular conformation, including the presence of D23−K28 salt bridges in the oligomers.

Madhu and co-workers investigated structural differences between A$\beta$40 fibrils and small oligomers formed at 25 $\mu$M A$\beta$40 concentration in volatile ammonium acetate buffer.[18a] $^{13}$C chemical shifts were found to be similar in residues 11−21 and 30−40 but significantly different in the N-terminal segment and in residues 23−28. F19−L34 crosspeaks were also observed, as discussed above, in 2D $^{13}$C ssNMR spectra of both fibrils and oligomers.

Härd and co-workers have reported ssNMR studies of protofibrils formed by a double cysteine mutant of A$\beta$42 in which a $\beta$-hairpin monomer conformation is enforced by an intramolecular disulfide linkage. From the ssNMR data and computational methods, they propose a structural model in which the protofibrils are stacks of A$\beta$42 hexamers with an overall $\beta$-barrel-like configuration. Although this is an intriguing model, it may not apply to unmodified A$\beta$ protofibrils.

Previous studies have examined A$\beta$ self-assembly intermediates that were prepared according to diverse protocols. In agreement with our data for high-pH, neutral-pH, and protofibril samples in frozen glycerol/water solutions, the molecular conformations in all intermediates resemble the conformations in A$\beta$40 and A$\beta$42 fibrils. Specifically, hydrophobic segments containing residues 17−21 and 30−36 (or somewhat longer segments) adopt extended, $\beta$-strand-like conformations. The N- and C-terminal extended segments are separated by a bend or loop, allowing them to interact with one another through side-chain−side-chain contacts (or possibly hydrogen bonds, in the case of self-assembly intermediates with $\beta$-hairpin conformations). However, it appears that most self-assembly intermediates do not contain the in-register, parallel $\beta$-sheet structure that has been found in all mature A$\beta$40 and A$\beta$42 fibrils to date.

Experiments described above are distinct from previous studies in that (1) we have characterized structural changes in a series of successive stages of the A$\beta$40 self-assembly process rather than focusing on a single species, (2) we have trapped transient species in frozen solution, and (3) we have used DNP to enhance the sensitivity of the ssNMR measurements, thereby avoiding the need for lyophilization.

**Prospects for Future Studies.** DNP-enhanced ssNMR measurements described above represent the first application of DNP to the structural characterization of transient or metastable species that are of biological relevance. Compared with earlier experiments on a protein-folding intermediate without DNP,[24c] the quantity of labeled peptide in each measurement was reduced by a factor of approximately 15 and the time required to acquire 2D $^{13}$C ssNMR spectra was reduced by factors of 10−30, depending on line widths. Thus, ssNMR experiments on transient states in a variety of processes become possible that were previously precluded by limitations on available protein quantities, solubility, and throughput.

Procedures for pH adjustment, mixing, and freezing employed in our experiments are slow, implying that self-assembly proceeds for at least several minutes before the neutral-pH samples are frozen for ssNMR measurements. In future studies, we plan to examine earlier stages of self-assembly following a rapid switch from solvent conditions under which A$\beta$ peptides are primarily monomeric to conditions that favor aggregation. Such studies will utilize rapid mixing and rapid freezing methods to trap intermediates on time scales ranging from milliseconds to seconds. With a similar approach, DNP-enhanced ssNMR studies of intermediates in protein folding, ligand binding, membrane insertion, and enzymatic processes are readily envisioned.

## ■ ASSOCIATED CONTENT

### Ⓢ Supporting Information

Additional data as described in the text. The Supporting Information is available free of charge on the ACS Publications website at DOI: 10.1021/jacs.5b04843.

## ■ AUTHOR INFORMATION

### Corresponding Author

*National Institutes of Health, Building 5, Room 112, Bethesda, MD 20892-0520. E-mail: robertty@mail.nih.gov. Phone: 301-402-8272.

### Notes

The authors declare no competing financial interest.

## ■ ACKNOWLEDGMENTS

This work was supported by the Intramural Research Program of the National Institute of Diabetes and Digestive and Kidney Diseases of the National Institutes of Health. A.P. was supported by a postdoctoral research fellowship from the Human Frontier Science Program.

## ■ REFERENCES

(1) (a) Glenner, G. G.; Wong, C. W. *Biochem. Biophys. Res. Commun.* **1984**, *120*, 885. (b) Hardy, J. A.; Higgins, G. A. *Science* **1992**, *256*, 184. (c) Dickson, D. W. *J. Neuropathol. Exp. Neurol.* **1997**, *56*, 321. (d) Karran, E.; Mercken, M.; De Strooper, B. *Nat. Rev. Drug Discovery* **2011**, *10*, 698.

(2) Terry, R. D.; Masliah, E.; Salmon, D. P.; Butters, N.; Deteresa, R.; Hill, R.; Hansen, L. A.; Katzman, R. *Ann. Neurol.* **1991**, *30*, 572.

(3) Hsia, A. Y.; Masliah, E.; McConlogue, L.; Yu, G. Q.; Tatsuno, G.; Hu, K.; Kholodenko, D.; Malenka, R. C.; Nicoll, R. A.; Mucke, L. *Proc. Natl. Acad. Sci. U.S.A.* **1999**, *96*, 3228.

(4) (a) Tycko, R.; Wickner, R. B. *Acc. Chem. Res.* **2013**, *46*, 1487. (b) Tycko, R. *Protein Sci.* **2014**, *23*, 1528.



DOI: 10.1021/jacs.5b04843
*J. Am. Chem. Soc.* 2015, 137, 8294−8307

(5) (a) Lu, J. X.; Qiang, W.; Yau, W. M.; Schwieters, C. D.; Meredith, S. C.; Tycko, R. *Cell* **2013**, *154*, 1257. (b) Petkova, A. T.; Leapman, R. D.; Guo, Z. H.; Yau, W. M.; Mattson, M. P.; Tycko, R. *Science* **2005**, *307*, 262. (c) Meyer-Luehmann, M.; Coomaraswamy, J.; Bolmont, T.; Kaeser, S.; Schaefer, C.; Kilger, E.; Neuenschwander, A.; Abramowski, D.; Frey, P.; Jaton, A. L.; Vigouret, J. M.; Paganetti, P.; Walsh, D. M.; Mathews, P. M.; Ghiso, J.; Staufenbiel, M.; Walker, L. C.; Jucker, M. *Science* **2006**, *313*, 1781. (d) Watts, J. C.; Condello, C.; Stohr, J.; Oehler, A.; Lee, J.; DeArmond, S. J.; Lannfelt, L.; Ingelsson, M.; Giles, K.; Prusiner, S. B. *Proc. Natl. Acad. Sci. U.S.A.* **2014**, *111*, 10323. (e) Cohen, M. L.; Kim, C.; Haldiman, T.; ElHag, M.; Mehndiratta, P.; Pichet, T.; Lissemore, F.; Shea, M.; Cohen, Y.; Chen, W.; Blevins, J.; Appleby, B. S.; Surewicz, K.; Surewicz, W. K.; Sajatovic, M.; Tatsuoka, C.; Zhang, S.; Mayo, P.; Butkiewicz, M.; Haines, J. L.; Lerner, A. J.; Safar, J. G. *Brain* **2015**, *138*, 1009.

(6) (a) Dickson, D. W.; Crystal, H. A.; Bevona, C.; Honer, W.; Vincent, I.; Davies, P. *Neurobiol. Aging* **1995**, *16*, 285. (b) Lesne, S.; Koh, M. T.; Kotilinek, L.; Kayed, R.; Glabe, C. G.; Yang, A.; Gallagher, M.; Ashe, K. H. *Nature* **2006**, *440*, 352. (c) Noguchi, A.; Matsumura, S.; Dezawa, M.; Tada, M.; Yanazawa, M.; Ito, A.; Akioka, M.; Kikuchi, S.; Sato, M.; Ideno, S.; Noda, M.; Fukunari, A.; Muramatsu, S.; Itokazu, Y.; Sato, K.; Takahashi, H.; Teplow, D. B.; Nabeshima, Y.; Kakita, A.; Imahori, K.; Hoshi, M. *J. Biol. Chem.* **2009**, *284*, 32895. (d) Lambert, M. P.; Barlow, A. K.; Chromy, B. A.; Edwards, C.; Freed, R.; Liosatos, M.; Morgan, T. E.; Rozovsky, I.; Trommer, B.; Viola, K. L.; Wals, P.; Zhang, C.; Finch, C. E.; Krafft, G. A.; Klein, W. L. *Proc. Natl. Acad. Sci. U.S.A.* **1998**, *95*, 6448.

(7) (a) Chromy, B. A.; Nowak, R. J.; Lambert, M. P.; Viola, K. L.; Chang, L.; Velasco, P. T.; Jones, B. W.; Fernandez, S. J.; Lacor, P. N.; Horowitz, P.; Finch, C. E.; Krafft, G. A.; Klein, W. L. *Biochemistry* **2003**, *42*, 12749. (b) Tay, W. M.; Huang, D. T.; Rosenberry, T. L.; Paravastu, A. K. *J. Mol. Biol.* **2013**, *425*, 2494. (c) Chimon, S.; Ishii, Y. *J. Am. Chem. Soc.* **2005**, *127*, 13472. (d) Chimon, S.; Shaibat, M. A.; Jones, C. R.; Calero, D. C.; Aizezi, B.; Ishii, Y. *Nat. Struct. Mol. Biol.* **2007**, *14*, 1157. (e) Hoshi, M.; Sato, M.; Matsumoto, S.; Noguchi, A.; Yasutake, K.; Yoshida, N.; Sato, K. *Proc. Natl. Acad. Sci. U.S.A.* **2003**, *100*, 6370. (f) Lasagna-Reeves, C. A.; Glabe, C. G.; Kayed, R. *J. Biol. Chem.* **2011**, *286*, 22122. (g) Ladiwala, A. R. A.; Litt, J.; Kane, R. S.; Aucoin, D. S.; Smith, S. O.; Ranjan, S.; Davis, J.; Van Nostrand, W. E.; Tessier, P. M. *J. Biol. Chem.* **2012**, *287*, 24765.

(8) (a) Harper, J. D.; Wong, S. S.; Lieber, C. M.; Lansbury, P. T. *Chem. Biol.* **1997**, *4*, 119. (b) Goldsbury, C.; Kistler, J.; Aebi, U.; Arvinte, T.; Cooper, G. J. S. *J. Mol. Biol.* **1999**, *285*, 33. (c) Williams, A. D.; Sega, M.; Chen, M. L.; Kheterpal, I.; Geva, M.; Berthelier, V.; Kaleta, D. T.; Cook, K. D.; Wetzel, R. *Proc. Natl. Acad. Sci. U.S.A.* **2005**, *102*, 7115. (d) Kheterpal, I.; Chen, M.; Cook, K. D.; Wetzel, R. *J. Mol. Biol.* **2006**, *361*, 785.

(9) Deshpande, A.; Mina, E.; Glabe, C.; Busciglio, J. *J. Neurosci.* **2006**, *26*, 6011.

(10) (a) Arispe, N.; Pollard, H. B.; Rojas, E. *Proc. Natl. Acad. Sci. U.S.A.* **1993**, *90*, 10573. (b) Lashuel, H. A.; Lansbury, P. T. *Q. Rev. Biophys.* **2006**, *39*, 167. (c) Demuro, A.; Mina, E.; Kayed, R.; Milton, S. C.; Parker, I.; Glabe, C. G. *J. Biol. Chem.* **2005**, *280*, 17294.

(11) (a) Yan, S. D.; Chen, X.; Fu, J.; Chen, M.; Zhu, H. J.; Roher, A.; Slattery, T.; Zhao, L.; Nagashima, M.; Morser, J.; Migheli, A.; Nawroth, P.; Stern, D.; Schmidt, A. M. *Nature* **1996**, *382*, 685. (b) Lauren, J.; Gimbel, D. A.; Nygaard, H. B.; Gilbert, J. W.; Strittmatter, S. M. *Nature* **2009**, *457*, 1128.

(12) (a) Huang, X. D.; Atwood, C. S.; Hartshorn, M. A.; Multhaup, G.; Goldstein, L. E.; Scarpa, R. C.; Cuajungco, M. P.; Gray, D. N.; Lim, J.; Moir, R. D.; Tanzi, R. E.; Bush, A. I. *Biochemistry* **1999**, *38*, 7609. (b) Barnham, K. J.; Masters, C. L.; Bush, A. I. *Nat. Rev. Drug Discovery* **2004**, *3*, 205. (c) Parthasarathy, S.; Long, F.; Miller, Y.; Xiao, Y. L.; McElheny, D.; Thurber, K.; Ma, B. Y.; Nussinov, R.; Ishii, Y. *J. Am. Chem. Soc.* **2011**, *133*, 3390.

(13) (a) Gonzalez-Scarano, F.; Baltuch, G. *Annu. Rev. Neurosci.* **1999**, *22*, 219. (b) Glass, C. K.; Saijo, K.; Winner, B.; Marchetto, M. C.; Gage, F. H. *Cell* **2010**, *140*, 918.

(14) Farkas, E.; Luiten, P. G. M. *Prog. Neurobiol.* **2001**, *64*, 575.

(15) (a) Petkova, A. T.; Yau, W. M.; Tycko, R. *Biochemistry* **2006**, *45*, 498. (b) Paravastu, A. K.; Leapman, R. D.; Yau, W. M.; Tycko, R. *Proc. Natl. Acad. Sci. U.S.A.* **2008**, *105*, 18349. (c) Bertini, I.; Gonnelli, L.; Luchinat, C.; Mao, J. F.; Nesi, A. *J. Am. Chem. Soc.* **2011**, *133*, 16013. (d) Niu, Z.; Zhao, W. J.; Zhang, Z. F.; Xiao, F. S.; Tang, X. Q.; Yang, J. *Angew. Chem., Int. Ed.* **2014**, *53*, 9294. (e) Schutz, A. K.; Vagt, T.; Huber, M.; Ovchinnikova, O. Y.; Cadalbert, R.; Wall, J.; Guntert, P.; Bockmann, A.; Glockshuber, R.; Meier, B. H. *Angew. Chem., Int. Ed.* **2015**, *54*, 331. (f) Sgourakis, N. G.; Yau, W. M.; Qiang, W. *Structure* **2015**, *23*, 216.

(16) (a) Benzinger, T. L. S.; Gregory, D. M.; Burkoth, T. S.; Miller-Auer, H.; Lynn, D. G.; Botto, R. E.; Meredith, S. C. *Proc. Natl. Acad. Sci. U.S.A.* **1998**, *95*, 13407. (b) Margittai, M.; Langen, R. *Q. Rev. Biophys.* **2008**, *41*, 265.

(17) (a) Tycko, R.; Sciarretta, K. L.; Orgel, J.; Meredith, S. C. *Biochemistry* **2009**, *48*, 6072. (b) Qiang, W.; Yau, W. M.; Tycko, R. *J. Am. Chem. Soc.* **2011**, *133*, 4018. (c) Qiang, W.; Yau, W. M.; Luo, Y. Q.; Mattson, M. P.; Tycko, R. *Proc. Natl. Acad. Sci. U.S.A.* **2012**, *109*, 4443.

(18) (a) Sarkar, B.; Mithu, V. S.; Chandra, B.; Mandal, A.; Chandrakesan, M.; Bhowmik, D.; Madhu, P. K.; Maiti, S. *Angew. Chem., Int. Ed.* **2014**, *53*, 6888. (b) Parthasarathy, S.; Inoue, M.; Xiao, Y.; Matsumara, Y.; Nabeshima, Y.; Hoshi, M.; Ishii, Y. *J. Am. Chem. Soc.* **2015**, *137*, 6480.

(19) (a) Scheidt, H. A.; Morgado, I.; Rothemund, S.; Huster, D.; Fandrich, M. *Angew. Chem., Int. Ed.* **2011**, *50*, 2837. (b) Scheidt, H. A.; Morgado, I.; Huster, D. *J. Biol. Chem.* **2012**, *287*, 22822.

(20) Ahmed, M.; Davis, J.; Aucoin, D.; Sato, T.; Ahuja, S.; Aimoto, S.; Elliott, J. I.; Van Nostrand, W. E.; Smith, S. O. *Nat. Struct. Mol. Biol.* **2010**, *17*, 561.

(21) Lopez del Amo, J. M.; Fink, U.; Dasari, M.; Grelle, G.; Wanker, E. E.; Bieschke, J.; Reif, B. *J. Mol. Biol.* **2012**, *421*, 517.

(22) Gu, L.; Liu, C.; Stroud, J. C.; Ngo, S.; Jiang, L.; Guo, Z. F. *J. Biol. Chem.* **2014**, *289*, 27300.

(23) Lendel, C.; Bjerring, M.; Dubnovitsky, A.; Kelly, R. T.; Filippov, A.; Antzutkin, O. N.; Nielsen, N. C.; Hard, T. *Angew. Chem., Int. Ed.* **2014**, *53*, 12756.

(24) (a) Havlin, R. H.; Tycko, R. *Proc. Natl. Acad. Sci. U.S.A.* **2005**, *102*, 3284. (b) Sharpe, S.; Kessler, N.; Anglister, J. A.; Yau, W. M.; Tycko, R. *J. Am. Chem. Soc.* **2004**, *126*, 4979. (c) Hu, K. N.; Yau, W. M.; Tycko, R. *J. Am. Chem. Soc.* **2010**, *132*, 24.

(25) (a) Petkova, A. T.; Buntkowsky, G.; Dyda, F.; Leapman, R. D.; Yau, W. M.; Tycko, R. *J. Mol. Biol.* **2004**, *335*, 247. (b) Tycko, R.; Hu, K. N. *J. Magn. Reson.* **2010**, *205*, 304. (c) Kloepper, K. D.; Hartman, K. L.; Ladror, D. T.; Rienstra, C. M. *J. Phys. Chem. B* **2007**, *111*, 13353.

(26) (a) Barnes, A. B.; De Paepe, G.; van der Wel, P. C. A.; Hu, K. N.; Joo, C. G.; Bajaj, V. S.; Mak-Jurkauskas, M. L.; Sirigiri, J. R.; Herzfeld, J.; Temkin, R. J.; Griffin, R. G. *Appl. Magn. Reson.* **2008**, *34*, 237. (b) Thurber, K. R.; Yau, W. M.; Tycko, R. *J. Magn. Reson.* **2010**, *204*, 303. (c) Thurber, K. R.; Tycko, R. *J. Chem. Phys.* **2012**, *137*, 084508. (d) Thurber, K. R.; Potapov, A.; Yau, W. M.; Tycko, R. *J. Magn. Reson.* **2013**, *226*, 100. (e) Hu, K. N.; Song, C.; Yu, H. H.; Swager, T. M.; Griffin, R. G. *J. Chem. Phys.* **2008**, *128*, 052302.

(27) (a) Bajaj, V. S.; Mak-Jurkauskas, M. L.; Belenky, M.; Herzfeld, J.; Griffin, R. G. *Proc. Natl. Acad. Sci. U.S.A.* **2009**, *106*, 9244. (b) Mao, J. F.; Do, N. N.; Scholz, F.; Reggie, L.; Mehler, M.; Lakatos, A.; Ong, Y. S.; Ullrich, S. J.; Brown, L. J.; Brown, R. C. D.; Becker-Baldus, J.; Wachtveitl, J.; Glaubitz, C. *J. Am. Chem. Soc.* **2014**, *136*, 17578. (c) Smith, A. N.; Caporini, M. A.; Fanucci, G. E.; Long, J. R. *Angew. Chem., Int. Ed.* **2015**, *54*, 1542.

(28) (a) Debelouchina, G. T.; Bayro, M. J.; van der Wel, P. C. A.; Caporini, M. A.; Barnes, A. B.; Rosay, M.; Maas, W. E.; Griffin, R. G. *Phys. Chem. Chem. Phys.* **2010**, *12*, 5911. (b) Bayro, M. J.; Debelouchina, G. T.; Eddy, M. T.; Birkett, N. R.; MacPhee, C. E.; Rosay, M.; Maas, W. E.; Dobson, C. M.; Griffin, R. G. *J. Am. Chem. Soc.* **2011**, *133*, 13967. (c) Potapov, A.; Thurber, K. R.; Yau, W. M.; Tycko, R. *J. Magn. Reson.* **2012**, *221*, 32.

(29) Sergeyev, I. V.; Day, L. A.; Goldbourt, A.; McDermott, A. E. *J. Am. Chem. Soc.* **2011**, *133*, 20208.



DOI: 10.1021/jacs.5b04843
*J. Am. Chem. Soc.* 2015, 137, 8294−8307

(30) (a) Bitan, G.; Lomakin, A.; Teplow, D. B. *J. Biol. Chem.* **2001**, *276*, 35176. (b) Bitan, G.; Kirkitadze, M. D.; Lomakin, A.; Vollers, S. S.; Benedek, G. B.; Teplow, D. B. *Proc. Natl. Acad. Sci. U.S.A.* **2003**, *100*, 330. (c) Lu, J. X.; Sharpe, S.; Ghirlando, R.; Yau, W. M.; Tycko, R. *Protein Sci.* **2010**, *19*, 1877.
(31) McKnight, C. J.; Doering, D. S.; Matsudaira, P. T.; Kim, P. S. *J. Mol. Biol.* **1996**, *260*, 126.
(32) Schneider, C. A.; Rasband, W. S.; Eliceiri, K. W. *Nat. Methods* **2012**, *9*, 671.
(33) Schuck, P.; Perugini, M. A.; Gonzales, N. R.; Howlett, G. J.; Schubert, D. *Biophys. J.* **2002**, *82*, 1096.
(34) Yau, W. M.; Thurber, K. R.; Tycko, R. *J. Magn. Reson.* **2014**, *244*, 98.
(35) Thurber, K. R.; Tycko, R. *J. Magn. Reson.* **2009**, *196*, 84.
(36) Delaglio, F.; Grzesiek, S.; Vuister, G. W.; Zhu, G.; Pfeifer, J.; Bax, A. *J. Biomol. NMR* **1995**, *6*, 277.
(37) (a) Morcombe, C. R.; Gaponenko, V.; Byrd, R. A.; Zilm, K. W. *J. Am. Chem. Soc.* **2004**, *126*, 7196. (b) Takegoshi, K.; Nakamura, S.; Terao, T. *Chem. Phys. Lett.* **2001**, *344*, 631.
(38) Qiang, W. *J. Magn. Reson.* **2011**, *213*, 171.
(39) Song, C. S.; Hu, K. N.; Joo, C. G.; Swager, T. M.; Griffin, R. G. *J. Am. Chem. Soc.* **2006**, *128*, 11385.
(40) (a) Qiang, W.; Kelley, K.; Tycko, R. *J. Am. Chem. Soc.* **2013**, *135*, 6860. (b) Kodali, R.; Williams, A. D.; Chemuru, S.; Wetzel, R. *J. Mol. Biol.* **2010**, *401*, 503.
(41) Golovchenko, N. P.; Kataeva, I. A.; Akimenko, V. K. *J. Chromatogr., A* **1992**, *591*, 121.
(42) (a) Fawzi, N. L.; Ying, J. F.; Ghirlando, R.; Torchia, D. A.; Clore, G. M. *Nature* **2011**, *480*, 268. (b) Walti, M. A.; Orts, J.; Vogeli, B.; Campioni, S.; Riek, R. *ChemBioChem* **2015**, *16*, 659.
(43) Wishart, D. S.; Bigam, C. G.; Holm, A.; Hodges, R. S.; Sykes, B. D. *J. Biomol. NMR* **1995**, *5*, 67.
(44) (a) Wishart, D. S.; Sykes, B. D.; Richards, F. M. *J. Mol. Biol.* **1991**, *222*, 311. (b) Spera, S.; Bax, A. *J. Am. Chem. Soc.* **1991**, *113*, 5490. (c) Saito, H. *Magn. Reson. Chem.* **1986**, *24*, 835.
(45) Sandberg, A.; Luheshi, L. M.; Sollvander, S.; de Barros, T. P.; Macao, B.; Knowles, T. P. J.; Biverstal, H.; Lendel, C.; Ekholm-Petterson, F.; Dubnovitsky, A.; Lannfelt, L.; Dobson, C. M.; Hard, T. *Proc. Natl. Acad. Sci. U.S.A.* **2010**, *107*, 15595.
(46) Luhrs, T.; Ritter, C.; Adrian, M.; Riek-Loher, D.; Bohrmann, B.; Doeli, H.; Schubert, D.; Riek, R. *Proc. Natl. Acad. Sci. U.S.A.* **2005**, *102*, 17342.
(47) Lansbury, P. T.; Costa, P. R.; Griffiths, J. M.; Simon, E. J.; Auger, M.; Halverson, K. J.; Kocisko, D. A.; Hendsch, Z. S.; Ashburn, T. T.; Spencer, R. G. S.; Tidor, B.; Griffin, R. G. *Nat. Struct. Biol.* **1995**, *2*, 990.


DOI: 10.1021/jacs.5b04843
*J. Am. Chem. Soc.* 2015, 137, 8294−8307